

Scaling relations and baryonic cycling in local star-forming galaxies

M. Ginolfi¹, L. K. Hunt², C. Tortora², R. Schneider³, and G. Cresci²

¹ Observatoire de Genève, Université de Genève, 51 Ch. des Maillettes, 1290 Versoix, Switzerland
e-mail: michele.ginolfi@unige.ch

² INAF/Osservatorio Astrofisico di Arcetri, Largo Enrico Fermi 5, I-50125 Firenze, Italy

³ Dipartimento di Fisica, Sapienza Università di Roma, Piazzale Aldo Moro 5, I-00185, Roma, Italy

Received XXX; accepted YYY

ABSTRACT

Metallicity and gas content are intimately related in the baryonic exchange cycle of galaxies, and galaxy evolution scenarios can be constrained by quantifying this relation. To this end, we have compiled a sample of 415 galaxies in the Local Universe, dubbed “MAGMA” (Metallicity And Gas for Mass Assembly), which covers an unprecedented range in parameter space, spanning more than 5 orders of magnitude in stellar mass (M_{star}), star-formation rate (SFR), and gas mass (M_{gas}), and a factor of ~ 60 in metallicity $[Z, 12+\log(\text{O}/\text{H})]$. We have applied 4-dimensional and 3-dimensional (3D) principal component analyses (PCAs) to our sample, to assess the true dimensionality of the data. In confirmation of previous work, we find that even with the vast parameter space covered by MAGMA, the relations between M_{star} , SFR, Z and M_{gas} ($M_{\text{HI}}+M_{\text{H}_2}$) require only two dimensions to describe the hypersurface. Nevertheless, to accommodate the curvature in the $M_{\text{star}}-Z$ relation, we have applied a piecewise 3D PCA that successfully predicts observed $12+\log(\text{O}/\text{H})$ to an accuracy of ~ 0.07 dex. We also present a new relation to express M_{gas} as a linear combination of M_{star} and SFR, to an accuracy of ~ 0.2 dex. Finally, for the first time on a statistically significant sample with all the necessary measurements, we quantify M_{gas} as a function of M_{star} and evaluate the effect of gas on the mass-metallicity relation (MZR). By inferring the metallicity-loading and mass-loading factors for the outflows produced by the MAGMA galaxies, we find that the metal-retention efficiency is not constant with M_{star} ; metals are expelled more efficiently from low-mass galaxies than from massive ones. Agreement with earlier work is excellent, but is highly sensitive to the values adopted for the stellar nucleosynthetic yield y . Our analysis shows clearly that gas content and outflows driven by star formation shape the MZR.

Key words. Galaxies: star formation – Galaxies: ISM – Galaxies: fundamental parameters – Galaxies: statistics – Galaxies: dwarfs – (ISM:) evolution

1. Introduction

As long as star formation occurs in their gas reservoirs, galaxies evolve increasing their stellar mass (M_{star}) and their metal content, depending on the relative efficiency of inflows/outflows, dynamical interactions, and environmental processes. In other words, at any time, M_{star} and metallicity (Z) reflect the combined effect of both the integrated history of star formation and the degree of interaction with the surrounding environment. Not surprisingly, the causal links between gas mass (M_{gas}), star formation rate (SFR), M_{star} , and Z , manifest in a number of observed correlations between these quantities, often referred to as *scaling relations*. Some among the most notable examples are: (i) the correlation between M_{star} and SFR (the so-called Main Sequence, MS; e.g., Brinchmann et al. 2004; Noeske et al. 2007; Daddi et al. 2010; Elbaz et al. 2011; Renzini & Peng 2015); (ii) the correlation between M_{gas} and SFR (the “Schmidt-Kennicutt”, SK, relation; e.g., Schmidt 1959; Kennicutt 1998; Bigiel et al. 2008; Leroy et al. 2009); and (iii) the “mass-metallicity relation”, MZR, between M_{star} and Z (e.g., Lequeux et al. 1979; Tremonti et al. 2004; Maiolino et al. 2008). In star-forming galaxies, Z is typically measured by the abundance of oxygen, O/H , in the ionized gas, as it is the most abundant heavy element produced by massive stars.

These scaling relations among fundamental properties of galaxies are potentially insightful tools to explore demographics of galaxies and their evolution. In particular, the mutual correlations among physical properties in galaxies imply that the observed residuals from the main relations (in other words, their intrinsic scatters) could be correlated with other variables. Many studies have investigated such a notion, and this type of analysis has proved to be a powerful diagnostic, providing simple quantitative tests for analytical models and numerical simulations.

Important clues come from systematic studies of the intrinsic scatter of the MZR, finding that a *fundamental metallicity relation* (FMR) exists between M_{star} , Z and SFR, that minimizes the scatter in the MZR (see e.g., Ellison et al. 2008; Mannucci et al. 2010). According to the FMR, galaxies lie on a tight, redshift-independent two-dimensional (2D) surface in 3D space defined by M_{star} , Z and SFR, where at a given M_{star} , galaxies with higher SFR have systematically lower gas-phase Z (see e.g., Hunt et al. 2012; Lara-López et al. 2013; Hunt et al. 2016a; Cresci et al. 2018). Many theoretical models have investigated this finding, explaining it in terms of an equilibrium between metal-poor inflows and metal-enriched outflows (e.g., Davé et al. 2012; Dayal et al. 2013; Lilly et al. 2013; Graziani et al. 2017).

Only recently, thanks to the growing number of available (atomic and molecular) gas mass measurements in galaxies, it has been possible to incorporate gas properties in studies of statistically significant samples. Observational results suggest that the FMR may be more strongly expressed via the gas mass rather than via the SFR (see e.g., [Bothwell et al. 2013](#); [Brown et al. 2018](#)). In this light, the FMR might be interpreted as a by-product of an underlying relationship between the scatter of the MZR and the gas content (e.g., [Zahid et al. 2014](#)). In particular, [Bothwell et al. \(2016b\)](#), with an analysis that included M_{star} , SFR, O/H, and molecular gas mass, M_{H_2} , found that the *true* FMR exists between M_{star} , O/H and M_{H_2} , which is linked to SFR via the SK star-formation law.

In this work we extend the studies described above, reporting the analysis of the mutual dependencies of physical properties in a sample of ~ 400 local galaxies, with simultaneous availability of M_{star} , SFR, M_{gas} (both atomic and molecular) and O/H, spanning an unprecedented range in M_{star} , extending down to $\sim 10^5 M_{\odot}$ at the low-mass end. Using a principle component analysis (PCA) technique, we explore the correlations in the 4D parameter space defined by M_{star} , SFR, O/H, and M_{gas} , especially focusing on the MZR scatter and the ramifications of including a significant population of low-mass galaxies in the sample. We also quantify properties of the inferred galaxy outflows, driven by star formation, and show that they have a strong impact on shaping the MZR.

2. Combined sample: MAGMA

We have compiled a sample of 415 local galaxies, with simultaneous availability of M_{star} , SFR, gas masses (both atomic, M_{HI} , and molecular, M_{H_2} , the latter obtained by measurements of CO luminosity, L'_{CO}) and metallicities $[12+\log(\text{O}/\text{H})]$. We assembled our sample by combining a variety of surveys at $z \sim 0$, following three selection criteria:

- (1) the combined sample includes *only* galaxies with robust ($\geq 3\sigma$) measurements/detections of M_{star} , SFR, $12+\log(\text{O}/\text{H})$, M_{HI} , and L'_{CO} ;
- (2) galaxies were eliminated if they were thought to host active galactic nuclei (AGN) based on the BPT classifications¹ provided by the original surveys;
- (3) properties of galaxies in common among two or more parent surveys have been taken from the sample that provided more ancillary information (e.g., high quality spectra, resolved maps, uniform derivation of parameters, etc.).

Because we require metallicity and gas measurements, we have dubbed our compiled sample MAGMA (Metallicity And Gas in Mass Assembly). The final MAGMA sample has been drawn from the following eight parent surveys/papers:

- **xGASS-CO:** xGASS-CO is the overlap between the extended GALEX Arcibo SDSS Survey (xGASS: [Catinella et al. 2018](#)) and the extended CO Legacy Database for GASS (xCOLD GASS: [Saintonge et al. 2017](#)). xGASS² is a gas fraction-limited census of the

HI gas content of ~ 1200 local galaxies, spanning over 2 decades in stellar mass ($M_{\star} = 10^9 - 10^{11.5} M_{\odot}$). The xCOLD GASS survey³ contains IRAM-30m CO(1-0) measurements for 532 galaxies also spanning the entire SFR – M_{\star} plane at $M_{\star} > 10^9 M_{\odot}$. Stellar masses are from the MPA-JHU⁴ catalogue, where M_{star} is computed from a fit to the spectral energy distribution (SED) obtained using SDSS broad-band photometry ([Brinchmann et al. 2004](#); [Salim et al. 2007](#)). SFRs are computed as described by [Janowiecki et al. \(2017\)](#) by combining NUV with mid-IR (MIR) fluxes from the Wide-field Infrared Survey Explorer (WISE; [Wright et al. 2010](#)). When these are not available (the case for $\sim 70\%$ of the xGASS sample), SFRs are determined using a “ladder” technique ([Janowiecki et al. 2017](#); [Saintonge et al. 2017](#)). Data Release 7 (SDSS DR7, [Abazajian et al. 2009](#)), calibrated by [Saintonge et al. \(2017\)](#) to the [NII]-based strong-line calibration by [Pettini & Pagel \(2004, PP04N2\)](#). In addition to omitting AGN and Seyferts (see above), we have also excluded galaxies in [Saintonge et al. \(2017\)](#) with an “undetermined” or “composite” classification, on the basis of the BPT diagram; metallicities from PP04N2 for such galaxies tend to be highly uncertain. xGASS-CO, the overlap between xGASS and xCOLDGASS, includes 477 galaxies, with 221 non-AGN galaxies with robust CO detections. The subset of xGASS-CO that respects our selection criteria (i.e., with HI and CO detections and not excluded for potentially uncertain O/H calibration) consists of **181** galaxies.

- **HRS:** The *Herschel* Reference Sample ([Boselli et al. 2010](#)) is a *K*-band selected, volume-limited sample comprising 323 galaxies. HRS⁵ is a fairly complete description of the Local Universe galaxy population although underrepresented in low-mass galaxies (see [Boselli et al. 2010](#)). Stellar masses M_{star} and SFRs were obtained from [Boselli et al. \(2015\)](#); M_{star} values were derived according to the precepts of [Zibetti et al. \(2009\)](#) using *i*-band luminosities and *g* – *i* colors, and SFRs were derived using $\text{H}\alpha$ luminosities corrected for dust extinction according to the prescriptions of [Calzetti et al. \(2010\)](#) which rely on $24\mu\text{m}$ emission. $12+\log(\text{O}/\text{H})$ was taken from [Hughes et al. \(2013\)](#) based on the PP04N2 calibration, and gas quantities, M_{HI} and L'_{CO} were taken from [Boselli et al. \(2014\)](#). **86** HRS galaxies have HI and CO detections, thus corresponding to our selection criteria.
- **KINGFISH:** The Key Insights on Nearby Galaxies: a Far-Infrared Survey with *Herschel*, KINGFISH⁶ ([Kennicutt et al. 2011](#)), contains 61 galaxies with metallicity in the range $7.54 \leq 12+\log(\text{O}/\text{H}) \leq 8.77$ and stellar masses in the range $[2 \times 10^7 - 1.4 \times 10^{11}] M_{\odot}$. Stellar masses and SFRs are taken from [Hunt et al. \(2019\)](#). The M_{star} values were computed from the SFR-corrected IRAC $3.6\mu\text{m}$ luminosities according to the luminosity-

³ The full xCOLD GASS survey data products are available on the xCOLD GASS website <http://www.star.ucl.ac.uk/xCOLDGASS/>.

⁴ <http://www.mpa.mpa-garching.mpg.de/SDSS/DR7/>

⁵ A full description of the survey and the ancillary data can be found at <https://hedam.lam.fr/HRS/>.

⁶ An overview of the scientific strategy for KINGFISH and the properties of the galaxy sample can be found on the web page <https://www.ast.cam.ac.uk/research/kingfish>.

¹ The Baldwin-Philips-Terlevich (BPT) diagram classification ([Baldwin et al. 1981](#)) relies on the emission-line properties of galaxies, based on the $[\text{SiII}]/\text{H}\alpha$ versus $[\text{OIII}]/\text{H}\beta$ ratios.

² The full xGASS representative sample is available on the xGASS website, <http://xgass.icrar.org> in digital format.

dependent mass-to-light (M/L) ratio given by Wen et al. (2013), and are within ~ 0.1 dex of those derived by comprehensive SED fitting (see Hunt et al. 2019). SFRs are inferred from the far-ultraviolet (FUV) luminosity combined with total-infrared (TIR) luminosity following Murphy et al. (2011). Atomic gas masses M_{HI} and CO measurements for M_{H_2} are taken from Kennicutt et al. (2011), with refinements from Sandstrom et al. (2013) and Aniano et al. (2019). Metallicities from Moustakas et al. (2010) were converted from the Kobulnicky & Kewley (2004, KK04) to the PP04N2 calibration according to the transformations given by Kewley & Ellison (2008); more details are given in Hunt et al. (2016a) and Aniano et al. (2019, in prep.). After omitting NGC 2841 and NGC 5055 because their metallicities exceeded the valid regime for the Kewley & Ellison (2008) algorithms, 38 KINGFISH galaxies respect our selection criteria, having HI and CO detections, and a reliable O/H determination.

- **ALLSMOG:** The APEX Low-redshift Legacy Survey of MOlecular Gas (Bothwell et al. 2014; Cicone et al. 2017) comprises 88 nearby, star-forming galaxies with stellar masses in the range $10^{8.5} < M_{\text{star}}/M_{\odot} < 10^{10}$, and gas-phase metallicities $12+\log(\text{O}/\text{H}) > 8.4$. ALLSMOG⁷ is entirely drawn from the MPA-JHU catalogue of spectral measurements and galactic parameters of SDSS DR7. Stellar mass and SFR values of ALLSMOG galaxies are taken from the MPA-JHU catalogue, and the SFR is based on the (aperture-corrected) H α intrinsic line luminosity. We have used the PP04N2 O/H calibration given by Cicone et al. (2017). The subset of ALLSMOG that respects our selection criteria consists of 38 galaxies.
- **NFGS:** The Nearby Field Galaxy Survey (Jansen et al. 2000; Kewley et al. 2005; Kannappan et al. 2009) consists of 196 galaxies spanning the entire Hubble sequence in morphological types, and a range in luminosities from low-mass dwarf galaxies to luminous massive systems. Stellar masses, M_{star} , are given by Kannappan et al. (2013) and are based on NUV+*ugriz*JHK+IRAC 3.6 μm SEDs. We have taken (spatially) integrated SFR (based on H α) and O/H values from Kewley et al. (2005), and transformed $12+\log(\text{O}/\text{H})$ from their Kewley & Dopita (2002, KD02) calibration to PP04N2 according to the formulations by Kewley & Ellison (2008). Stark et al. (2013) provides CO and M_{H_2} measurements, and M_{HI} is tabulated by Wei et al. (2010) and Kannappan et al. (2013). After removing NGC 7077, that appears in the following dwarf sample, there are 24 galaxies that meet our selection criteria.
- **BCDs:** The Blue Compact Dwarf galaxies (BCDs) have been observed and detected in $^{12}\text{CO}(1-0)$ with the IRAM 30m single dish (Hunt et al. 2015, 2017). They were selected primarily from the primordial helium sample of Izotov et al. (2007), known to have reliable metallicities $12+\log(\text{O}/\text{H})$ measured through the direct electron-temperature (T_e) method. An additional, similar, set of BCDs has been detected in $^{12}\text{CO}(1-0)$ (Hunt et al. 2019, in prep.) with analogous selection criteria. Stellar masses and SFRs are taken from Hunt

et al. (2015). M_{star} is derived as for KINGFISH galaxies, namely from IRAC 3.6 μm or WISE 3.4 μm luminosities, after correcting for free-free, line emission based on SFR, and dust continuum when possible. This method has been shown to be consistent with full-SED derived M_{star} values to within $\lesssim 0.1$ dex (Hunt et al. 2019). For the galaxy in common with the NFGS, NGC 7077, the two M_{star} estimates are the same to within 0.07 dex. SFRs are based on the Calzetti et al. (2010) combination of H α and 24 μm luminosities. HI masses are given by Hunt et al. (2015) and Hunt et al. (2019, in prep.). As mentioned above, $12+\log(\text{O}/\text{H})$ is obtained from the direct T_e method (for details see Hunt et al. 2016a). The subset of BCDs that respect our selection criteria with HI and CO [$^{12}\text{CO}(1-0)$] detections comprises 17 galaxies with metallicities $12+\log(\text{O}/\text{H})$ ranging from 7.7 to 8.4; to our knowledge, this is the largest sample of low-metallicity dwarf galaxies in the Local Universe detected in CO.

- **DGS:** The Dwarf Galaxy Survey, DGS⁸ (Madden et al. 2013, 2014), is a *Herschel* sample of 48 local metal-poor low-mass galaxies, with metallicities ranging from $12+\log(\text{O}/\text{H}) = 7.14$ to 8.43 and stellar masses from 3×10^6 to $\sim 3 \times 10^{10} M_{\odot}$. The DGS sample was originally selected from several deep optical emission line and photometric surveys including the Hamburg/SAO Survey and the First and Second Byurakan Surveys (e.g., Ugryumov et al. 1999, 2003; Markarian & Stepanian 1983; Izotov et al. 1991). Although stellar masses are given by Madden et al. (2013) with corrected values in Madden et al. (2014), these are calculated according to Eskew et al. (2012) using the Spitzer/IRAC luminosities at 3.6 μm and 4.5 μm . Hunt et al. (2016a) gives M_{star} for these same galaxies by first subtracting nebular continuum and line emission, known to be important in metal-poor star-forming dwarf galaxies (e.g., Smith & Hancock 2009); a comparison shows that the M_{star} values in Madden et al. (2014) are, on average, 0.3 dex larger than those by Hunt et al. (2016a). Thus, in order to maximize consistency with the other samples considered here, like for the KINGFISH, BCDs, and the Virgo star-forming dwarfs (see below), we have used stellar masses based on WISE and/or IRAC 3.4-3.6 μm luminosities using the recipe by Wen et al. (2013) after subtracting off non-stellar emission estimated from the SFR (see also Hunt et al. 2012, 2015, 2019). Metallicities for the DGS are taken from De Vis et al. (2017), using their PP04N2 calibration. We have also recalculated the SFRs using H α and 24 μm luminosities as advocated by Calzetti et al. (2010) and reported in Hunt et al. (2016a). Of the 48 DGS galaxies discussed by Rémy-Ruyer et al. (2014), 7 are included in the BCD sample observed in CO by Hunt et al. (2015, 2017); 5 have CO detections from Cormier et al. (2014); and 9 elsewhere in the literature (Kobulnicky et al. 1995; Young et al. 1995; Greve et al. 1996; Walter et al. 2001; Leroy et al. 2005, 2006; Gratier et al. 2010; Schrubba et al. 2012; Oey et al. 2017). However, one of these, UM 311, is a metal-poor HII region within a larger galaxy (see Hunt et al. 2010). There is a discrepancy between the M_{star} values given by Madden

⁷ The full ALLSMOG survey data products are available on the web page <http://www.mrao.cam.ac.uk/ALLSMOG/>.

⁸ Information on the DGS sample, as well as data products, can be found on the website <http://irfu.cea.fr/Pisp/diane.cormier/dgsweb/publi.html>.

et al. (2014) and Hunt et al. (2016a) of more than a factor of 100; this is roughly the difference between the larger UM 311 complex and the individual metal-poor HII regions, illustrating that the gas content of the individual HII regions is highly uncertain. We thus eliminate UM 311 from the DGS subset, and include the remaining 13 DGS galaxies that respect our selection criteria.

- **Virgo star-forming dwarfs:** This sample of star-forming dwarf galaxies (SFDs) in Virgo is taken from a larger survey, namely the *Herschel* Virgo Cluster Survey, HeViCS⁹ (Davies et al. 2010). Here to supplement the low-mass portion of our combined sample, we have included the dwarf galaxies in HeViCS studied by Grossi et al. (2015, 2016). They were selected from the larger sample by requiring a dwarf morphology (e.g., Sm, Im, BCD) and detectable far-infrared (FIR) emission with *Herschel*. M_{star} was estimated according to the WISE 3.4 μm luminosities, and SFRs were calculated using H α luminosities and correcting for dust using WISE 22 μm emission as proposed by Wen et al. (2014). Both quantities are originally given with a Kroupa (2001) initial mass function (IMF), and have been corrected here to a Chabrier (2003) IMF according to Speagle et al. (2014). Metallicities, $12+\log(\text{O}/\text{H})$, were based on the SDSS spectroscopy and use the PP04N2 calibration reported by Grossi et al. (2016), with the exception of VCC 1686 for which O/H was derived using the mass-metallicity relation given in Hughes et al. (2013). Of 20 targets observed, 11 were detected in $^{12}\text{CO}(1-0)$ with the IRAM 30m (Grossi et al. 2016). Atomic hydrogen HI is detected in all these (Grossi et al. 2016), so that the subset of HeViCS that respects our selection criteria consists of 11 galaxies.
- **Extra single sources:** This subset includes individual galaxies that are not included in any survey, but for which our required data of M_{star} , SFR, O/H, CO, and HI measurements exist. These include 7 low-metallicity galaxies: DDO 53 and DDO 70 (Sextans B) from Shi et al. (2016), NGC 3310 (Zhu et al. 2009), NGC 2537 (Gil de Paz et al. 2002), WLM (Elmegreen et al. 2013), Sextans A (Shi et al. 2015), NGC 2403 Schrupa et al. (2012). For these sources, as above for consistency, we used M_{star} and SFR from Hunt et al. (2016a). We were able to compare global M_{star} for one of these, WLM, and once reported to a common distance scale, our value of M_{star} agrees with that from Elmegreen et al. (2013) to within 0.1 dex. Metallicities for these objects are based on the direct T_e method, and taken from Engelbracht et al. (2008), Marble et al. (2010), and Berg et al. (2012). In the following figures, the 5 galaxies from these additional sources are labeled as “Extra”.

2.1. Detailed properties and potential selection effects

All stellar masses and star-formation rates are calculated according to a Chabrier (2003) IMF, or, if necessary, converted to this IMF according to Speagle et al. (2014). As mentioned in the previous section, all gas-phase metallicities in our combined sample are either direct T_e methods or

calibrated through the [NII]-based PP04N2 Pettini & Pagel (2004) calibration.

Like metallicity, molecular gas mass is another delicate issue. Except for ALLSMOG, we use only CO(1–0) so avoid excitation issues; to convert the ALLSMOG CO(2–1) values from Ciccone et al. (2017) to CO(1–0), we assume $R_{21} = 0.8$ as they advocate. The molecular gas masses have been calculated from the L'_{CO} , using the conversion $M_{\text{H}_2} = L'_{\text{CO}} \alpha_{\text{CO}}$ (where α_{CO} is the H_2 mass-to-CO light conversion factor), and adopting a metallicity-dependent calibration, following Hunt et al. (2015). Specifically, for galaxies with $Z/Z_{\odot} < 1$ (i.e., $12+\log(\text{O}/\text{H}) < 8.69$, see Asplund et al. 2009), we applied $\alpha_{\text{CO}} = \alpha_{\text{CO}_{\odot}} (Z/Z_{\odot})^{-1.96}$; for metallicities $Z/Z_{\odot} \geq 1$ we used a constant solar value of $\alpha_{\text{CO}} = \alpha_{\text{CO}_{\odot}} = 3.2 M_{\odot} (\text{K km s}^{-1} \text{pc}^2)^{-1}$.

We have also investigated the effect of adopting the strong-line metallicity formulation by Kewley & Dopita (2002, KD02), and the α_{CO} formulation from Wolfire et al. (2010); this last assumes that the α_{CO} varies exponentially with visual extinction, A_V , with a weak metallicity dependence for A_V (see Bolatto et al. 2013, for more details). These results will be discussed in Sect. 4.1.

The M_{star} distributions of our combined sample are shown in Fig. 1, while the specific SFR ($\text{sSFR} \equiv \text{SFR}/M_{\text{star}}$), Z [measured in units of $12+\log(\text{O}/\text{H})$] gas fractions $M_{\text{gas}}/(M_{\text{gas}} + M_{\text{star}})$ distributions are shown in Fig. 2. The combined MAGMA sample covers the following unprecedented ranges in parameter space, spanning more than 5 orders of magnitude in M_{star} , SFR, and M_{gas} , and almost 2 orders of magnitude in metallicity¹⁰:

$$5.2 \lesssim \log(M_{\text{star}}/M_{\odot}) \lesssim 11.3$$

$$5.4 < \log(M_{\text{gas}}/M_{\odot}) < 10.8$$

$$-4.5 \lesssim \log(\text{SFR}/M_{\odot} \text{ yr}^{-1}) \lesssim 1.6$$

$$7.5 \lesssim 12 + \log(\text{O}/\text{H}) \lesssim 9.3$$

To demonstrate the general applicability of results obtained for MAGMA to the general galaxy population in the Local Universe, we have included in Figs. 1 and 2 the parameter distributions for the SDSS-DR7 catalogue consisting of 78579 galaxies from Mannucci et al. (2010); hereafter we refer to this sample as SDSS10. For a consistent comparison with MAGMA, like for the samples described above, we have transformed the original O/H calibration from Maiolino et al. (2008) based on KD02 to PP04N2 according to the formulation of Kewley & Ellison (2008) (for more details, see also Hunt et al. 2016a); according to Kewley & Ellison (2008), this transformation has an accuracy of ~ 0.05 dex. The distributions shown in Figs. 1 and 2 have been renormalized to the number of galaxies in the MAGMA sample, so as to be able to compare the number distributions directly. The SDSS10 has a relatively narrow spread in O/H; there are 5 MAGMA galaxies ($\sim 1\%$) beyond the highest metallicities in SDSS10, and all are from the xCOLDGASS sample, corresponding also to some of the most massive galaxies. The MAGMA M_{star} median is 0.6 dex lower than for the SDSS10, and the sSFR median (Fig. 2) is ~ 0.4 dex higher, illustrating that the MAGMA sample contains more low-mass galaxies than SDSS10. Interestingly, there are only 25 SDSS10 galaxies (0.03%) with

⁹ Information on HeViCS and public data can be found in <http://wiki.arcetri.astro.it/HeViCS/WebHome>.

¹⁰ Here and elsewhere throughout this paper, “log” means decimal logarithm unless otherwise noted.

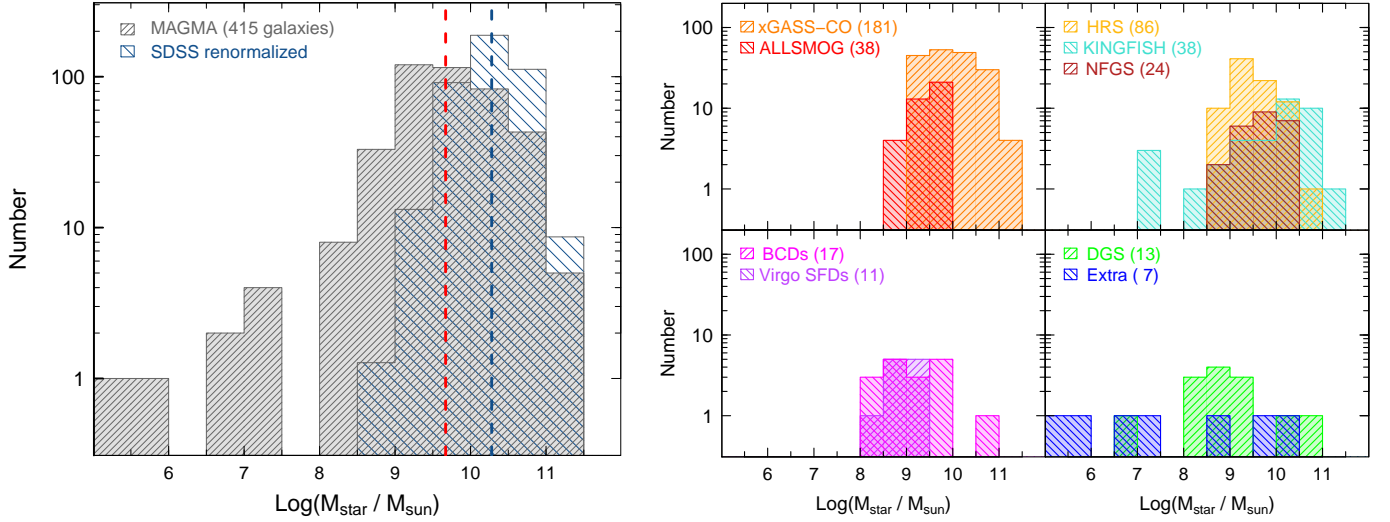


Fig. 1. Distributions of M_{star} for the MAGMA sample; the right panels illustrate the subdivisions in M_{star} for the parent surveys. The vertical dashed line in the left panel corresponds to the median M_{star} for MAGMA, $\log(M_{\text{star}}/M_{\odot})=9.68$. Also shown in the left panel is the SDSS10 sample, taken from Mannucci et al. (2010), consisting of 78579 galaxies. Here it has been renormalized to show the M_{star} distribution it would have were it to comprise the same number of galaxies (415) as MAGMA; the M_{star} median of SDSS10 is $\log(M_{\text{star}}/M_{\odot})=10.28$.

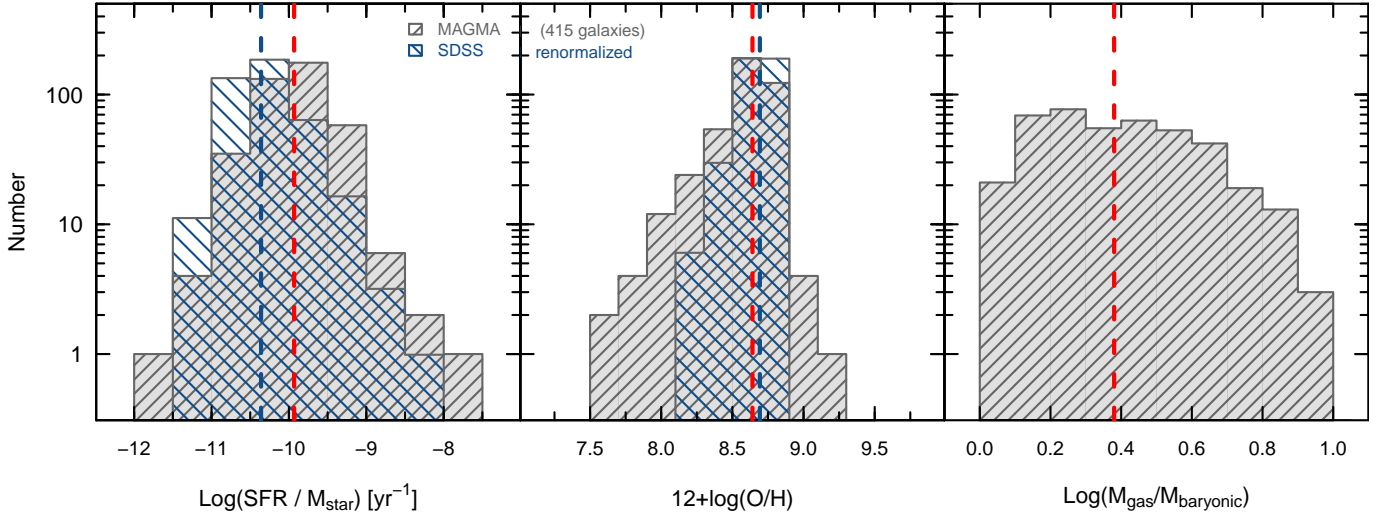


Fig. 2. Distributions for combined sample of 415 galaxies for $\log(\text{sSFR} \equiv \text{SFR}/M_{\text{star}})$ (left panel), $12+\log(\text{O}/\text{H})$ (middle), and $\log[M_{\text{gas}}/(M_{\text{star}} + M_{\text{gas}}) \equiv M_{\text{gas}}/M_{\text{baryonic}}]$ (right). The vertical dashed lines in each panel corresponds to the MAGMA medians: $\log(\text{sSFR}/\text{yr}^{-1})=-9.93$; $12+\log(\text{O}/\text{H})=8.64$ (Z_{\odot} would be $12+\log(\text{O}/\text{H})=8.69$, see Asplund et al. 2009); $\log(M_{\text{gas}}/M_{\text{baryonic}})=\log(f_{\text{baryonic}})=0.38$. Also shown in the left panel is the SDSS10 sample, as in Fig. 1; the sSFR and O/H medians of SDSS10 are $\log(\text{sSFR}/\text{yr}^{-1})=-10.36$, and $12+\log(\text{O}/\text{H})=8.69$, respectively.

$\log(M_{\text{star}}/M_{\odot}) > 11.5$; thus because of the normalization in Fig. 1 they do not appear.

Both MAGMA and SDSS10 contain a large percentage of massive galaxies relative to local volume-limited samples such as the Local Volume Legacy (e.g., LVL, Dale et al. 2009; Kennicutt et al. 2009) or galaxy-stellar mass functions (GSMF). For the $z \sim 0$ GSMF determined by Baldry et al. (2012) we would expect $\sim 0.1\%$ of the galaxies to be more massive than the break mass, $M_{*} = 5 \times 10^{10}$; $\sim 14\%$ of the galaxies in SDSS10 and $\sim 6\%$ of those in MAGMA are more massive than this. The preponderance of massive galaxies in these two samples, relative to a volume-limited one, is due to flux limits, and the necessity of ensuring spectroscopic measurements (for SDSS10) and CO measurements

(for MAGMA). In any case, as shown in Figs. 1 and 2, the parameter coverage of MAGMA does not deviate significantly from SDSS10 at high M_{star} and O/H, but extends substantially the parameter space to lower M_{star} and O/H values.

Given that we required that CO be *detected*, even at low metallicity, there could be a chance that the MAGMA sample is dominated by starbursts, i.e., galaxies with SFRs significantly above the main sequence. We examine this possibility in Fig. 3, where we compare the distributions for MAGMA galaxies of SFR in different bins of M_{star} with the SDSS10 data from Mannucci et al. (2010) as above. There is also the main sequence of star formation given by fitting LVL and KINGFISH by Hunt et al. (2019), here

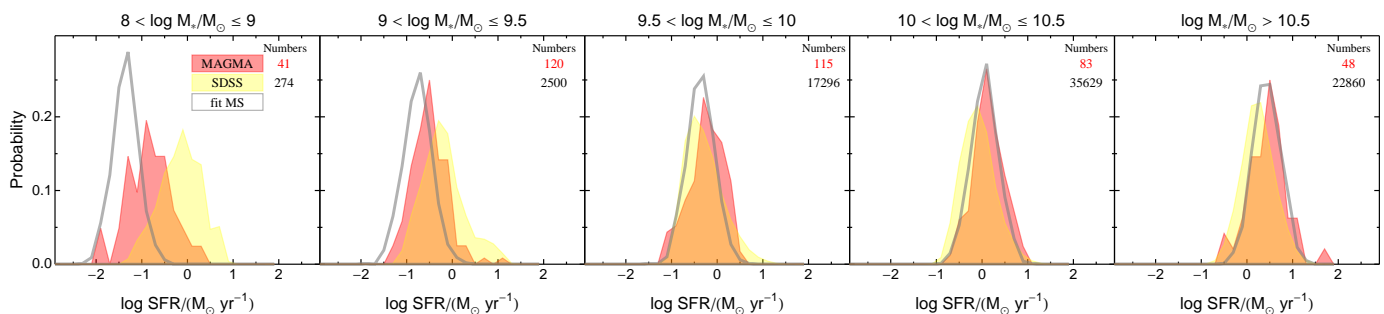


Fig. 3. Distributions of SFR for the MAGMA sample shown as red-shaded regions in bins of M_{star} ; also shown are the SDSS10 sample in yellow-shaded regions, and the fit to the SFMS (shown as a solid grey curve) reported by [Hunt et al. \(2019\)](#). The close agreement of MAGMA with SDSS and the SFMS, except possibly for the lowest M_{star} bin, suggests that starbursts are not dominating the galaxy population represented.

approximated by a Gaussian distribution with a width of 0.3 dex (see also [Renzini & Peng 2015](#)). Except for possibly the lowest-mass bins, $\log(M_{\text{star}}/M_{\odot}) \leq 9$, Fig. 3 demonstrates that the MAGMA sample is well approximated by main-sequence SFR distributions. Thus, it is not dominated by starbursts, and can be considered a reliable diagnostic for gas processes in the Local Universe.

2.2. Fundamental scaling relations

In Fig. 4, MAGMA galaxies are plotted in the M_{star} -SFR plane, forming the so-called main sequence; the lower panels of Fig. 4 show various forms of the correlation between SFR and M_{gas} , exploring different gas phases (atomic, molecular and total, i.e., $M_{\text{HI}}+M_{\text{H}_2}$) and CO luminosity, L'_{CO} . Also shown in Fig. 4 are the loci of the SDSS10 galaxies reported in previous figures. The lowest-level contour encloses 90% of the sample, illustrating the extension by MAGMA to lower M_{star} and SFR. We have included in Fig. 4 also the parameters from the LVL sample as measured by [Hunt et al. \(2016a\)](#); most metallicities are from the direct T_{e} method ([Marble et al. 2010](#); [Berg et al. 2012](#)). This sample is the best approximation available for the number and type of galaxies present in the nearby Universe.

Figure 5 shows the mass-metallicity ($M_{\text{star}}-Z$) relation of the MAGMA sample; although with some scatter, galaxies lie along the MZR over > 4 dex in M_{star} and a factor of ~ 50 in Z (1.7 dex in $12+\log(\text{O}/\text{H})$). As in Fig. 4, we have also included SDSS10 and LVL; the MAGMA sample is consistent with both, implying that there are no significant selection effects from our gas detection requirements. Also shown as a blue curve in Fig. 5 is the direct- T_{e} calibration for the SDSS obtained by [Andrews & Martini \(2013\)](#); the MAGMA PP04N2+direct T_{e} metallicities are in good agreement with this calibration illustrating that PP04N2 is a good approximation to T_{e} methods (see also [Hunt et al. 2016a](#)).

Fig. 5 illustrates that the flattening of the MZR that frequently emerges at high M_{star} is present in the MAGMA and SDSS10 samples. This curvature is clearly seen in the contours of SDSS10 where 90% of the SDSS10 galaxies are enclosed in the lowest contour. Again, the overall extension of MAGMA to lower M_{star} and O/H is evident. In what follows, we focus on applying linear scaling relations to this curved MZR. A single linear relation is not altogether appropriate, given the flattening of the MZR at high M_{star} . Indeed, as shown by the linear trend in the upper panel of Fig.

5, it can only roughly approximate the overall MAGMA distribution. In what follows, we investigate the best approach to approximate non-linear trends in the data.

A combination of the scaling relations described above produce the result reported in the lower panel of Fig. 5, namely a tight correlation between the specific SFR ($\text{sSFR} = \text{SFR}/M_{\text{star}}$) and metallicity over ~ 2 dex in sSFR and \lesssim dex in $12+\log(\text{O}/\text{H})$. Fig. 5 demonstrates that galaxies more actively forming stars (i.e., with a high sSFR) are less enriched (and also more gas-rich; see [Mannucci et al. 2010](#); [Cresci et al. 2012](#); [Hunt et al. 2016b](#); [Cresci et al. 2018](#), for a discussion).

In the next section we focus on the MZR (Fig. 5), exploring its secondary and tertiary dependencies on SFR and M_{H_2} , M_{HI} , and M_{gas} . Since Z is the only *intensive*¹¹ quantity among the available integrated physical properties of our galaxies, the MZR is, among the others described above, the most sensitive to internal physical mechanisms.

3. Mutual correlations: a PCA analysis

Principal Component Analysis (PCA) is a parameter transformation technique that diagonalizes the covariance matrix of a set of variables. Consequently, a PCA gives the linear combinations of observables, the eigenvectors, that define the orientations whose projections constitute a hyper-plane; these eigenvectors minimize the covariance and are, by definition, mutually orthogonal. In other words, a PCA performs a coordinate transformation that identifies the optimum projection of a dataset and the parameters that are most responsible for the variance in the sample. The most common use of PCA is to search for possible *dimensionality reduction* of the parameter space needed to describe a dataset. For instance, a PCA approach has shown that galaxies lie roughly on a 2D surface in the 3D parameter space defined by M_{star} , SFR and Z (e.g., [Hunt et al. 2012, 2016a](#)) or M_{star} , M_{H_2} and Z (e.g., [Bothwell et al. 2016a](#)).

Here we perform two distinct sets of PCAs: (1) on a 4-dimensional (4D) parameter space defined by M_{star} , SFR, Z , and a gas quantity (either M_{gas} , M_{H_2} , M_{HI} , or L'_{CO}); and (2)

¹¹ Intensive properties are physical properties of a system that do not depend on the system size or the amount of material in the system (e.g., the metallicity of a galaxy does not depend on its size). They differ from *extensive* properties, that are additive for subsystems. For instance, the total M_{star} , M_{gas} and SFR in a galaxy are the sums of the parts composing the galaxy; in other words these quantities depend on the size of a galaxy.

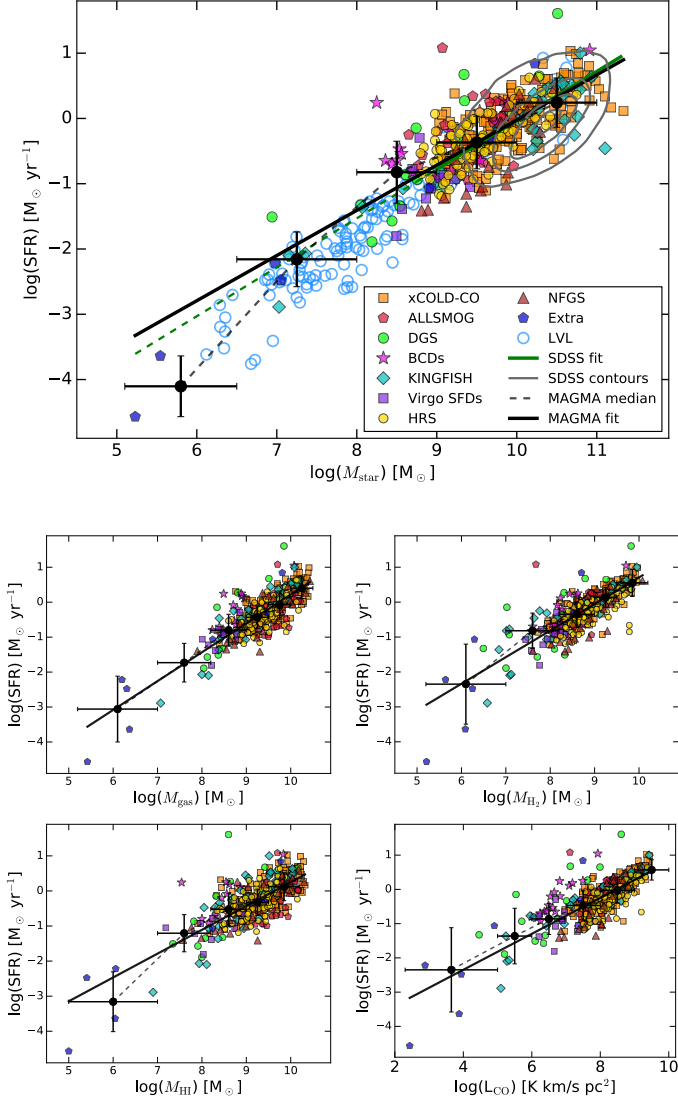


Fig. 4. Upper panel: Galaxies from the MAGMA sample plotted in the $\text{SFR}-M_{\text{star}}$ plane. The green dashed line is the MS of star-forming galaxies derived from the SDSS (Brinchmann et al. 2004); it is shown as a solid line over the region defined by the SDSS, and the extrapolation to the MAGMA parameter range by a dashed line. Contours in this plane for the SDSS10 sample are shown as grey closed curves; the lowest-level contour encloses 90% of the sample. Also shown in both panels is the LVL sample (Dale et al. 2009; Kennicutt et al. 2009) as described in the text. Lower panels: MAGMA galaxies in the $\text{SFR}-M_{\text{gas}}$ (upper-left), M_{H_2} -SFR (upper-right), M_{HI} -SFR (lower-left), and L'_{CO} -SFR (lower-right) planes. Symbols and colours refer to different parent surveys, as indicated in the legend. In all panels, the black dashed lines represent the median trends of the MAGMA distributions, calculated at different bins (see black dots; horizontal bars indicate the widths of the bins, while vertical bars indicate the standard deviation around median values of galaxies in the bins). The grey solid lines represent a linear fit to the distributions.

on a 3-dimensional (3D) space defined by M_{star} , SFR, and either metallicity Z or a gas quantity (as for 4D). We then assess whether two, three, or four parameters are statistically necessary to describe the variance of these quantities in the MAGMA sample. We have included L'_{CO} as a separate gas quantity in order to separate the effects of true CO

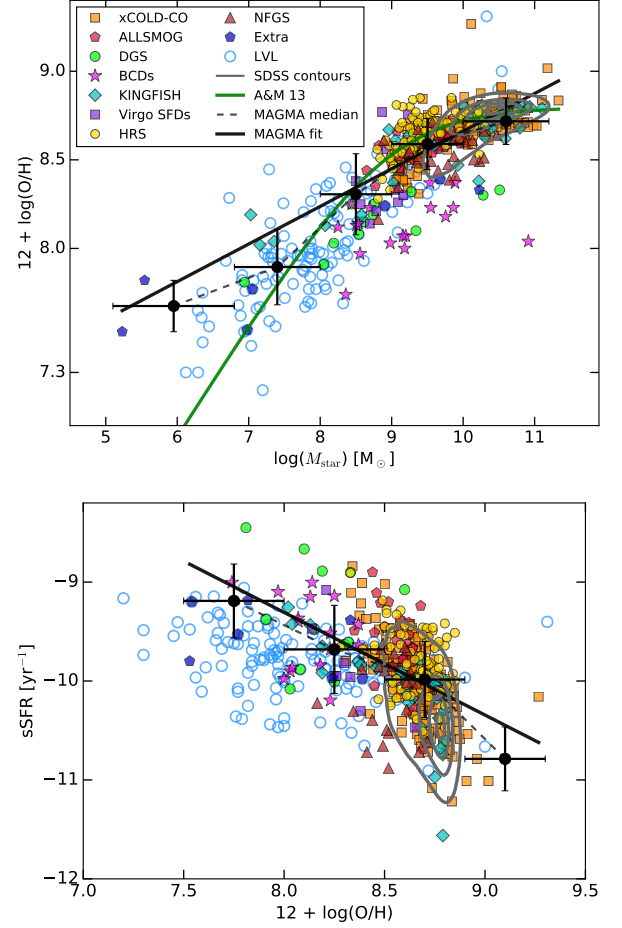


Fig. 5. Upper panel: the MAGMA sample in the $M_{\text{star}}-Z$ plane; lower panel: MAGMA sample in the $\text{sSFR}-Z$ plane. Metallicities are reported in PP04N2 (or T_{e}) units of $12+\log(\text{O}/\text{H})$. In both panels, as in previous figures, the SDSS10 sample is also plotted, with 90% of the galaxies enclosed within the lowest contours; both panels show also the LVL sample (Dale et al. 2009; Kennicutt et al. 2009) as described in the text. In the upper panel, the MZR from the direct- T_{e} determination by Andrews & Martini (2013) is also given, and its good agreement with the MAGMA PP04N2 ($+T_{\text{e}}$) metallicities suggests that the calibrations are consistent. Symbols and colours refer to different parent surveys, as indicated in the legend. The black dashed line represents the median trend of the distribution, calculated at different bins (see black dots; horizontal bars indicate the widths of the bins, while vertical bars indicate the standard deviation around median values of galaxies in the bins).

luminosity from the effects of a metallicity-dependent α_{CO} ; this point will be discussed further below.

In addition to the “classical” algorithm for PCA (an unweighted matrix diagonalization), we also apply two additional PCA methods which give the uncertainties associated with the best-fit parameters: the “bootstrap PCA” (BSPCA) first introduced by Efron (1979, 1982) and the “probabilistic PCA” (PPCA) described by Roweis (1998). BSPCA is a specific example of more generic techniques that resample the original data set with replacement, to construct “independent and identically distributed” observations; and PPCA is an expectation-maximization (EM) algorithm which also accommodates missing information. For the PPCA, we randomly remove 5% of the individual

entries for each galaxy; in practice, this means that we omit the SFR for 5% of the galaxies, M_{star} for a different 5%, and so on. For both methods, we generate 1000 repetitions, and calculate the means and standard deviations of the resulting PC coefficients. For all statistical analysis, we rely on the R statistical package¹².

To estimate uncertainties, other groups have used Monte Carlo methods with resampling, injecting Gaussian noise into the nominal measurement values (e.g., Bothwell et al. 2016a,b). We performed several detailed tests using this technique and found that it introduces systematics in the results, depending on the amplitude of the noise and the M_{star} and SFR distributions of the samples; hence we prefer resampling techniques in order to avoid potential unreliability of the results. This point will be discussed further in Sect. 4.3 and Appendix B.

3.1. 4D PCA

Results for the 4D PCA are given in Table 1; the coefficients of the PC with the least variance (by definition PC4) are reported, together with the fraction of variance contained in PC4, PC3, and the sum of PC1+PC2. There are two rows each for the PPCA and the BSPCA; these correspond to different realizations of the methods, and demonstrate that the coefficients of all the methods agree to within the uncertainties. We find that the proportion of variance contained in only the first two eigenvectors, PC1+PC2, is generally large, $\sim 92 - 94\%$. Because most of the variance of the sample is contained within the first two eigenvectors, the dimensionality of the parameter space of the MAGMA galaxies is two-fold. They are distributed on a 2D plane in the 4D space; the remaining $\sim 6-8\%$ of the variance (shared between PC3 and PC4) produces a scatter perpendicular to this plane.

PC4, the eigenvector with the least variance ($\sim 1\%$), is always dominated by metallicity, Z (see Table 1). Because very little of the sample variance is contained in PC4, it can be set to zero and inverted to give a useful prediction for the dominant term, namely metallicity Z (see Hunt et al. 2012, 2016a, for a discussion). The estimate for the metallicity obtained by setting PC4 equal to zero is formally accurate to the 1–2% level, i.e., the variance associated with PC4; however, a more robust assessment of the accuracy is obtained by fitting the residuals to a Gaussian as described below.

Interestingly, the contribution to PC4 of most of the gas parameters (M_{HI} , M_{H_2} , M_{gas}) is very little (consistent with 0.0 within the $\sim 2\sigma$ errors); the only gas component with a PC4 coefficient statistically different from 0 is L'_{CO} , with a coefficient determined at $\sim 8\sigma$. From inspection of Table 1, it can be seen that the coefficients for PC4 of PC4(1) [$12+\log(\text{O}/\text{H})$], PC4(2) [$\log(M_{\text{star}})$], and PC4(3) [$\log(\text{SFR})$] are virtually identical to within the errors, independently of which gas component is considered (again with the exception of L'_{CO}). This result implies that the 2D plane does not depend on gas properties (except for possibly CO luminosity L'_{CO}). The expression for $12+\log(\text{O}/\text{H})$ obtained by

inverting the expression based on M_{H_2} is:

$$o = (0.31 \pm 0.025)m - (0.16 \pm 0.04)s - (0.04 \pm 0.03)h_2 \quad (1)$$

where h_2 , m , o , and s are defined as the centered variables, i.e., $\log(M_{\text{H}_2})$, $\log(M_{\text{star}})$, $12+\log(\text{O}/\text{H})$, and $\log(\text{SFR})$ minus their respective means in the MAGMA sample as given in Table 2. The accuracy of this expression is ~ 0.096 dex, assessed by fitting a Gaussian to the residuals of this fit compared to the observations of $12+\log(\text{O}/\text{H})$. Eq. (1), in which the uncertainties from Table 1 have been propagated, tells us that:

- the gas-phase metallicity of galaxies in the MAGMA sample is primarily dependent on M_{star} (a confirmation of the existence of the well known MZR);
- there is a strong secondary dependence on the SFR, whose contribution in determining Z is $\gtrsim 50\%$ as strong as the dependence on M_{star} ;
- the tertiary dependence on M_{H_2} is negligible, virtually zero, given that the accuracy with which the coefficient is determined is $\sim 1\sigma$.

We have explored the behavior of the other gas quantities, and as suggested by Table 1, it is similar to the behavior of H_2 ; with the possible exception of L'_{CO} , the gas content is not influencing metallicity Z . However, in the case of L'_{CO} , the M_{star} coefficient is significantly smaller than that for the other gas quantities and the L'_{CO} coefficient has the same sign. It seems that, in some sense, the CO content (not necessarily the H_2 content which depends also on metallicity as we have inferred it, see Sect. 2.1) is linked to Z , and can partially substitute the influence of M_{star} . If we express $12+\log(\text{O}/\text{H})$ in terms of L'_{CO} , as we have done in Eq. (1), we obtain:

$$o = (0.12 \pm 0.03)m - (0.20 \pm 0.03)s + (0.20 \pm 0.02)\ell \quad (2)$$

where o , m , s are as in Eq. (1), and ℓ is the centered variable $\log(L'_{\text{CO}})$. This expression is accurate to ~ 0.09 dex assessed, as above for M_{H_2} , by fitting a Gaussian to the residuals of the fit. In reality, this fit should not be interpreted rigorously, since the gas content, rather than CO luminosity, is the quantity of interest. The relation between L'_{CO} and the molecular gas content is almost entirely governed by metallicity (e.g., Hunt et al. 2015; Accurso et al. 2017), thus the strong dependence by L'_{CO} in Eq. (2) is a reflection of the strong metallicity dependence of the conversion factor α_{CO} ; we will further explore this notion more in details in a future paper.

3.2. 3D PCA

Section 3.1 showed that the 4D parameter space can be approximated by a planar surface; $\sim 92-94\%$ of the variance is contained in the first two eigenvectors, PC1+PC2. Here we examine the 3D parameter space (in log space) by retaining M_{star} and SFR as the two main observables, and considering $12+\log(\text{O}/\text{H})$ as one of the variables together with the four gas quantities described above: M_{HI} , M_{H_2} , M_{gas} , and L'_{CO} . The aim of this exercise is to assess whether any of the gas parameters can be described only by M_{star} and SFR, and to

¹² R is a free software environment for statistical computing and graphics (<https://www.r-project.org/>).

Table 1. 4D PCA results for MAGMA^a

Method	PC4(1) 12+log(O/H) (PP04N2) (1)	PC4(2) log ($M_{\text{star}}/M_{\odot}$) (3)	PC4(3) log (SFR/ $M_{\odot}\text{yr}^{-1}$) (4)	PC4(4) log(x) (5)	PC4 std. dev. (6)	PC4 proportion of variance (7)	PC3 proportion of variance (8)	PCA1+PC2 proportion of variance (9)
PCA	0.941	-0.290	0.168	$x = M_{\text{HI}}/M_{\odot}$ -0.050	0.138	0.015	0.071	0.914
PPCA	0.957 ± 0.006	-0.257 ± 0.013	0.127 ± 0.019	-0.047 ± 0.013	0.14	0.02		
PPCA	0.955 ± 0.005	-0.260 ± 0.010	0.129 ± 0.016	-0.047 ± 0.012	0.14	0.02		
BSPCA	0.940 ± 0.011	-0.291 ± 0.019	0.168 ± 0.030	-0.051 ± 0.019	0.14	0.015		
BSPCA	0.939 ± 0.012	-0.291 ± 0.020	0.170 ± 0.033	-0.050 ± 0.020	0.14	0.015		
PCA	0.944	-0.293	0.149	$x = M_{\text{H2}}/M_{\odot}$ -0.022	0.139	0.015	0.064	0.921
PPCA	0.959 ± 0.005	-0.257 ± 0.017	0.115 ± 0.019	-0.031 ± 0.019	0.15	0.02		
PPCA	0.958 ± 0.006	-0.258 ± 0.018	0.113 ± 0.019	-0.031 ± 0.120	0.14	0.02		
BSPCA	0.939 ± 0.012	-0.296 ± 0.025	0.160 ± 0.038	-0.035 ± 0.025	0.14	0.015		
BSPCA	0.942 ± 0.011	-0.292 ± 0.024	0.151 ± 0.038	-0.035 ± 0.024	0.14	0.015		
PCA	0.940	-0.283	0.179	$x = M_{\text{gas}}/M_{\odot}$ -0.071	0.138	0.016	0.062	0.923
PPCA	0.955 ± 0.006	-0.251 ± 0.015	0.137 ± 0.021	-0.065 ± 0.022	0.14	0.02		
PPCA	0.955 ± 0.007	-0.250 ± 0.016	0.137 ± 0.024	-0.067 ± 0.021	0.14	0.02		
BSPCA	0.939 ± 0.015	-0.282 ± 0.021	0.176 ± 0.044	-0.069 ± 0.033	0.14	0.016		
BSPCA	0.938 ± 0.012	-0.283 ± 0.020	0.180 ± 0.038	-0.070 ± 0.033	0.14	0.016		
PCA	0.957	-0.118	0.185	$x = L'_{\text{CO}}/M_{\odot} (\text{K km s}^{-1} \text{pc}^2)^{-1}$ -0.190	0.113	0.008	0.051	0.941
PPCA	0.966 ± 0.004	-0.118 ± 0.021	0.153 ± 0.014	-0.169 ± 0.016	0.12	0.01		
PPCA	0.966 ± 0.003	-0.121 ± 0.021	0.154 ± 0.014	-0.167 ± 0.015	0.12	0.01		
BSPCA	0.955 ± 0.008	-0.115 ± 0.025	0.188 ± 0.026	-0.194 ± 0.018	0.11	0.008		
BSPCA	0.956 ± 0.008	-0.118 ± 0.027	0.187 ± 0.025	-0.190 ± 0.020	0.11	0.008		
Method	PC4(1) 12+log(O/H) (KD02)	PC4(2) log ($M_{\text{star}}/M_{\odot}$)	PC4(3) log (SFR/ $M_{\odot}\text{yr}^{-1}$)	PC4(4) log (M_{H2}/M_{\odot}) ^b	PC4 std. dev.	PC4 variance	PC3 variance	PCA1+PC2 variance
PCA	0.923	-0.286	0.223	-0.127	0.172	0.021	0.067	0.911
PPCA	0.944 ± 0.009	-0.245 ± 0.033	0.173 ± 0.022	-0.128 ± 0.027	0.179	0.024		
PPCA	0.942 ± 0.008	-0.253 ± 0.030	0.178 ± 0.023	-0.124 ± 0.026	0.178	0.024		
BSPCA	0.919 ± 0.020	-0.272 ± 0.054	0.231 ± 0.045	-0.142 ± 0.048	0.170	0.021		
BSPCA	0.920 ± 0.022	-0.277 ± 0.058	0.225 ± 0.048	-0.133 ± 0.049	0.170	0.021		

^a In PCA, the relative signs of the PCs are arbitrary, so that we have used the same conventions for all; this has no bearing on the inversion of the equation of the PC with the least variance. Column (6) reports the standard deviation of PC4 around the hyperplane, and Cols. (7–9) give the proportion of sample variance contained in PC4, PC3, and the sum of PC1+PC2, respectively.

^b Here M_{H2} is calculated from α_{CO} according to the exponential formulation of [Wolfire et al. \(2010\)](#); [Bolatto et al. \(2013\)](#), using the KD02 metallicities.

investigate the implication of our 4D PCAs that metallicity 12+log(O/H) can be adequately described by M_{star} and SFR alone.

Using the same methodology as for the 4D PCA (“classic” PCA without uncertainties, PPCA and BSPCA with uncertainties), we have performed 3D PCAs on the MAGMA sample, and obtain the results reported in Table 3. Like the 4D PCA, the 3D-PCA component with the least variance is dominated by the metallicity, 12+log(O/H) (see column 4 in Table 3). Inverting the PC3 dominated by O/H as before for the 4D PCA, we find:

$$o = (0.32 \pm 0.02)m - (0.14 \pm 0.03)s \quad (3)$$

The coefficients multiplying $\log(M_{\text{star}})$ and $\log(\text{SFR})$ in Eq. (3) are the same to within the uncertainties as those from the 4D PCA given in Eq. (1). This expression describes 12+log(O/H) for the MAGMA sample with an accuracy of ~ 0.1 dex, again obtained by fitting the residuals to a Gaussian. However, the MAGMA slope for $\log(M_{\text{star}})$ is shallow, significantly shallower than the 0.37 slope found by [Hunt et al. \(2016a\)](#).

There are two considerations here: one is that a PCA, by definition, must pass through the multi-variable centroid of the dataset. That is why here, in contrast to [Hunt et al. \(2012\)](#) and [Hunt et al. \(2016a\)](#), we have defined the PCA results in terms of centered variables. This is important

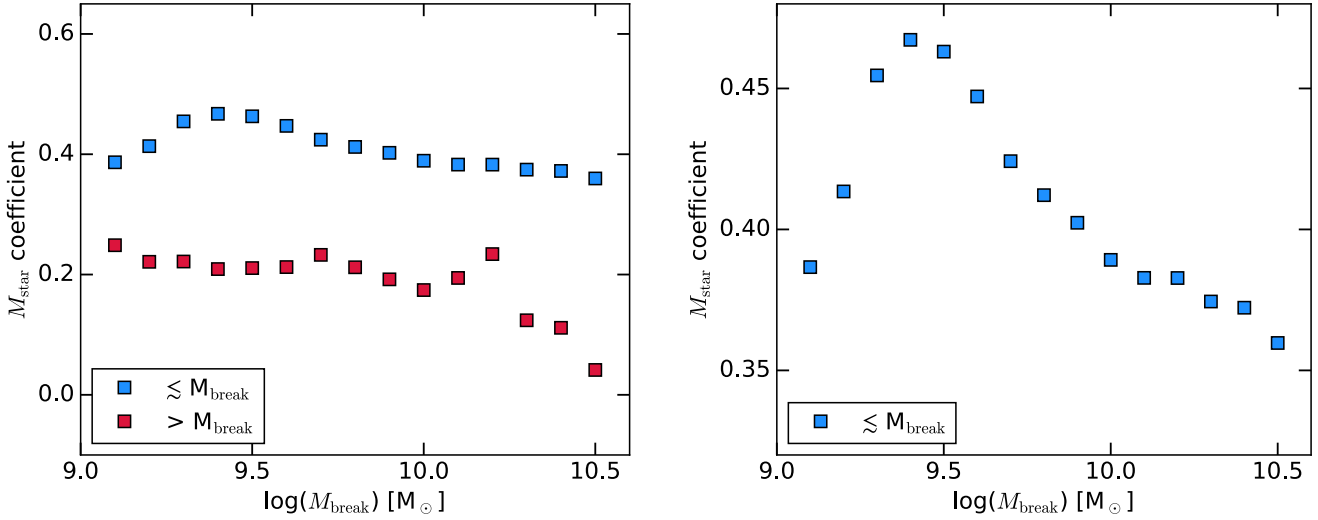


Fig. 6. PCA coefficients for MAGMA $\log(M_{\text{star}})$ plotted against M_{break} for the division into the two PCAs. The right panel is a magnification of the left panel, showing more effectively the range of M_{star} coefficients as the M_{break} mass is varied. The lower values of the M_{star} coefficient toward higher M_{break} results from the flattening of the MZR at high M_{star} .

Table 2. MAGMA sample means

Quantity (1)	Mean ^a (for $M_{\text{star}} \leq M_{\text{break}}^b$) (2)	Std. dev. (for $M_{\text{star}} > M_{\text{break}}$) (3)	Mean (4)	Mean (5)
$\log(M_{\text{star}}/M_{\odot})$	9.650	0.74	9.453	10.640
$\log(\text{SFR}/M_{\odot} \text{ yr}^{-1})$	-0.266	0.64	-0.397	0.391
$12+\log(\text{O}/\text{H})$	8.588	0.22	8.559	8.733
$\log(M_{\text{HI}}/M_{\odot})$	9.240	0.70	9.140	9.741
$\log(M_{\text{H2}}/M_{\odot})$	8.721	0.68	8.574	9.458
$\log(M_{\text{gas}}/M_{\odot})$	9.413	0.64	9.302	9.970
$\log(L'_{\text{CO}}/M_{\odot} (\text{K km s}^{-1} \text{ pc}^2)^{-1})$	7.965	0.95	7.776	8.911

^a The number of galaxies considered in the mean for Cols. (2,3) is 415, for Col. (4) 346, and for Col. (5) 69.

^b $M_{\text{break}} = 2 \times 10^{10} M_{\odot}$ (see also Fig. 6).

when applying a PCA determined with one sample to another sample; if the means of the two samples are significantly different, then the PCA will not pass through the barycenter of the data for the second sample, and will apparently not be a good fit. *Thus a PCA must be applied using centered variables.* The second consideration is that the curvature present in MAGMA (and SDSS10) is more pronounced than for the sample analyzed by [Hunt et al. \(2016a\)](#). Thus, the shallower slope found for MAGMA reflects the behavior more at the high-mass end than at the low-mass one; Fig. 6 shows the coefficient of M_{star} for the subsample with $M_{\text{star}} \leq M_{\text{break}}$ and $M_{\text{star}} > M_{\text{break}}$. The slopes for M_{star} are systematically smaller for increasing M_{break} , because of the flattening of the MZR. In the following section, we explore a remedy for this using an approach more appropriate for data showing non-linear relationships.

3.2.1. 3D PCA, a non-linear approach

Several methods have been developed to assess mutual dependencies and dimensionality in a dataset that shows non-linear behavior. In particular, curvature in a dataset can be first approximated by a piecewise linear approach (e.g., [Hastie & Stuetzle 1989](#); [Strange & Zwiggelaar 2015](#); [Xianxi](#)

Table 3. 3D PCA results for MAGMA^a

Method (1)	PC3(1) $\log(M_{\text{star}}/M_{\odot})$ (2)	PC3(2) $\log(\text{SFR}/M_{\odot} \text{ yr}^{-1})$ (3)	PC3(3) (4)	PC3 std. dev. (5)	PC3 variance (6)
PCA	0.302	-0.137	$12+\log(\text{O}/\text{H})$ -0.944	0.139	0.023
PPCA	0.270 ± 0.013	-0.101 ± 0.017	-0.958 ± 0.005	0.15	0.03
PPCA	0.270 ± 0.013	-0.100 ± 0.019	-0.958 ± 0.005	0.15	0.03
BSPCA	0.297 ± 0.022	-0.130 ± 0.032	-0.945 ± 0.011	0.14	0.02
BSPCA	0.302 ± 0.021	-0.138 ± 0.028	-0.943 ± 0.010	0.14	0.02
PCA	0.475	-0.841	$\log(M_{\text{HI}}/M_{\odot})$ 0.260	0.291	0.069
PPCA	0.468 ± 0.032	-0.842 ± 0.006	0.264 ± 0.044	0.30	0.08
PPCA	0.466 ± 0.033	-0.842 ± 0.006	0.266 ± 0.043	0.30	0.08
BSPCA	0.479 ± 0.062	-0.833 ± 0.019	0.258 ± 0.077	0.29	0.07
BSPCA	0.477 ± 0.060	-0.836 ± 0.016	0.254 ± 0.077	0.29	0.07
PCA	0.010	-0.758	$\log(M_{\text{H2}}/M_{\odot})$ 0.653	0.283	0.066
PPCA	0.112 ± 0.083	-0.759 ± 0.068	0.628 ± 0.080	0.30	0.08
PPCA	0.127 ± 0.105	-0.759 ± 0.082	0.617 ± 0.100	0.30	0.08
BSPCA	0.233 ± 0.193	-0.668 ± 0.198	0.633 ± 0.148	0.28	0.06
BSPCA	0.223 ± 0.177	-0.687 ± 0.189	0.623 ± 0.152	0.28	0.06
PCA	0.146	-0.780	$\log(M_{\text{gas}}/M_{\odot})$ 0.608	0.266	0.062
PPCA	0.130 ± 0.063	-0.774 ± 0.023	0.615 ± 0.042	0.28	0.07
PPCA	0.137 ± 0.061	-0.774 ± 0.023	0.613 ± 0.043	0.28	0.07
BSPCA	0.141 ± 0.085	-0.767 ± 0.044	0.615 ± 0.074	0.26	0.06
BSPCA	0.149 ± 0.084	-0.767 ± 0.052	0.611 ± 0.080	0.26	0.06
PCA	0.823	-0.446	$\log(L'_{\text{CO}}/M_{\odot} (\text{K km s}^{-1} \text{ pc}^2)^{-1})$ -0.351	0.287	0.052
PPCA	0.788 ± 0.038	-0.543 ± 0.086	-0.264 ± 0.079	0.31	0.06
PPCA	0.786 ± 0.042	-0.541 ± 0.094	-0.267 ± 0.084	0.31	0.06
BSPCA	0.799 ± 0.072	-0.441 ± 0.169	-0.347 ± 0.118	0.29	0.05
BSPCA	0.806 ± 0.048	-0.440 ± 0.144	-0.347 ± 0.114	0.28	0.05

^a As in Table 1, the relative signs of the PCs are arbitrary, so that we have used the same conventions for all; this has no bearing on the inversion of the equation of the PC with the least variance. Similarly to Table 1, Column (5) reports the standard deviation of PC3 around the hyperplane, and Col. (6) gives the proportion of its sample variance.

[et al. 2017](#)). In the case of the curved MZR and its relation with SFR (e.g., [Mannucci et al. 2010](#); [Cresci et al. 2018](#)), this is a fairly good approximation as we show below. The fit to the MZR given by [Andrews & Martini \(2013\)](#), shown in Fig. 5, consists of a mainly linear portion toward low M_{star} , connected smoothly to a roughly flat regime at high M_{star} . Thus, as a simplified solution to the problem of MZR

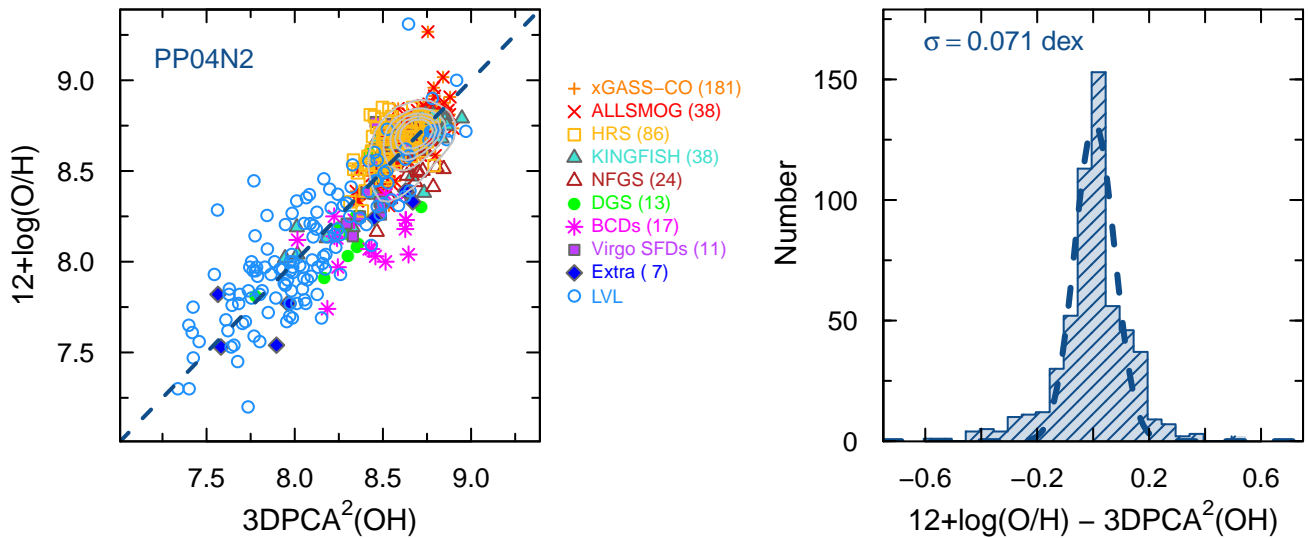


Fig. 7. Observed values of $12+\log(\text{O}/\text{H})$ in the MAGMA sample to those predicted by the $3\text{DPCA}^2(\text{OH})$ given in Eq. (4). The parent sample of the individual MAGMA galaxies is given in the legend in the middle panel, and the right panel shows the residuals and the Gaussian fit; the 1σ dispersion of the Gaussian is 0.071 dex as discussed in the text. Also shown is the MAGMA $3\text{DPCA}^2(\text{OH})$ applied to SDSS10, as before with 90% of SDSS10 enclosed within the contours. The mean SDSS10 residuals relative to the $\{3\text{DPCA}^2(\text{OH})\}$ are 0.007 dex, with a standard deviation of ~ 0.09 dex, showing that even with the MZR curvature clearly evident in SDSS10, the MAGMA $3\text{DPCA}^2(\text{OH})$ does a reasonable job of reproducing the metallicities (see text for more details).

curvature, we approximate its behavior with two linear segments, and perform a PCA separately on each. Such a procedure is a specific example of a more complex piecewise linear approach, and we postpone a more detailed analysis to a future paper.

The only “free parameter” in the piecewise linear PCA exercise is the break mass, M_{break} , namely the value of M_{star} where we establish the transition from one PCA to the other. We have investigated M_{break} between $3 \times 10^9 M_{\odot}$ and $3 \times 10^{10} M_{\odot}$ (see Fig. 6) and find a “sweet spot” around $M_{\text{break}} = 2 \times 10^{10} M_{\odot}$, where the overall variance is minimized. The best-fit piecewise 3D-PCA for MAGMA is as follows:

$$o = \begin{cases} (0.38 \pm 0.02)m - (0.15 \pm 0.03)s & \text{if } \log(M_{\text{star}}/M_{\odot}) \leq 10.3 \\ (0.12 \pm 0.06)m - (0.18 \pm 0.06)s & \text{if } \log(M_{\text{star}}/M_{\odot}) > 10.3 \end{cases} \quad (4)$$

and the averages of the parameters in the two bins are given in Table 2.

Figure 7 shows the piecewise 3D-PCA results [hereafter “ $3\text{DPCA}^2(\text{OH})$ ”] where we compare the predictions of $12+\log(\text{O}/\text{H})$ from Eq. (4) and the means given above to the observed values (vertical axis). The parent samples of the individual MAGMA galaxies are given in the legend in the middle panel. The standard deviation of the PC3 component is smaller (0.07 dex vs. ~ 0.1 dex) than that in the metallicity-dominated 4D PCA with, however, gas content taken into account. The Gaussian fit to the $3\text{DPCA}^2(\text{OH})$ residuals is shown in the right panel of Fig. 7, and is superior to the 4D PCA.

Also reported in Fig. 7 is the SDSS10 sample, to which we have applied the $3\text{DPCA}^2(\text{OH})$ determined from MAGMA; the grey contours enclose 90% of the sample. The mean (median) SDSS10 residuals are 0.000 (0.007) dex with a standard deviation of 0.09 dex over 78579 galaxies. Thus the MAGMA $3\text{DPCA}^2(\text{OH})$ applied to

SDSS10 represents the metallicities in that sample with accuracy better than 0.1 dex and with low systematics given the zero mean. For LVL, the scatter is slightly worse: mean (median) LVL residuals are 0.000 (-0.02) dex, with a standard deviation of ~ 0.2 dex over 135 galaxies. Nevertheless, the small mean (median) residuals indicate that the LVL metallicities are also fairly well approximated by the MAGMA $3\text{DPCA}^2(\text{OH})$.

Ultimately, the 4D PCAs show that there is no need to include gas content, either M_{gas} , M_{HI} , or M_{H_2} , in the description of Z ; it is statistically irrelevant, since a similar scatter is obtained without any gas coefficient. **This is a clear confirmation that metallicity in galaxies in the Local Universe can be determined to $\lesssim 0.1$ dex accuracy using only M_{star} and SFR.** However, it is not a statement that metallicity is independent of gas content; on the contrary, in Sect. 5, we describe how gas content shapes the MZR through star-formation-driven outflows. As we shall see below, the point is that gas content, like metallicity, can be described through M_{star} and SFR dependencies.

4. Comparison with previous work

Our results are in stark contrast with those of Bothwell et al. (2016b) who, as mentioned above, in a 4D PCA found that H_2 mass had a stronger link with metallicity than SFR. Bothwell et al. (2016a) found a similar result based on a 3D PCA, namely that gas content drives the relation between M_{star} and metallicity, and that any tertiary dependence on SFR is merely a consequence of the Schmidt-Kennicutt relation between gas mass and SFR. In a similar vein, Brown et al. (2018) through stacking and Bothwell et al. (2013) found that HI mass is strongly tied to Z , more strongly than SFR, similarly to later results for M_{H_2} . We conclude,

instead, that metallicity is more tightly linked with stellar mass and SFR than with either M_{gas} , M_{HI} , or even M_{H_2} . There are several possible reasons for this disagreement, and we explore them here, with additional details furnished in Appendix A.

4.1. Metallicity calibration and CO luminosity-to-molecular gas mass conversion

We first examine how our results change if we use the same metallicity calibration as Bothwell et al. (2016a,b). This is potentially an important consideration because the KD02 O/H calibration used by Bothwell et al. tends to give metallicities that are too high (e.g., Kewley & Ellison 2008), relative to direct- T_e estimates; as shown in Fig. 5, the PP04N2 is a better approximation of these (Andrews & Martini 2013; Hunt et al. 2016a; Curti et al. 2017). Together with using the KD02 calibration, we have also assessed the effect of applying the α_{CO} conversion factor used by Bothwell et al.; the exponential metallicity dependence proposed by Wolfire et al. (2010); Bolatto et al. (2013) depends more steeply on metallicity than the power-law dependence we have used above, as formulated by Hunt et al. (2015). Thus it is possible that the effects of metallicity are enhanced for the molecular gas mass M_{H_2} with the combination of these two parameters.

We have thus applied these calibrations to the MAGMA sample, and perform a 4D PCA, as in Bothwell et al. (2016b). The results of this exercise are reported in the lower portion of Table 1. With the KD02 calibration and the exponential metallicity dependence of α_{CO} , we find that the PC4 coefficients for O/H and M_{star} are virtually unchanged, the SFR coefficient is somewhat larger, but the M_{H_2} coefficient is 4 times larger. Thus, with the KD02 O/H calibration and for α_{CO} calculated according to Wolfire et al. (2010), our results for the O/H, M_{H_2} , and M_{star} coefficients for the MAGMA sample are more similar to those found by Bothwell et al. (2016b). Nevertheless, MAGMA galaxies show a larger SFR dependence than found by them, and even larger than the M_{H_2} coefficient, so that we would not have concluded that SFR has a negligible impact relative to H_2 .

4.2. Differences in sample sizes and properties

Here we examine whether the larger MAGMA sample, its significant low-mass representation, and different SFR relations can influence PCA results. Our MAGMA sample of 415 galaxies is nominally twice as large as the sample studied by Bothwell et al. (2016a,b). However, if we consider only the CO detections in their low- z sample (141 galaxies), judging from Table 2 in Bothwell et al. (2016a), our sample is roughly three times larger. Moreover, MAGMA contains a much larger fraction of low-mass galaxies, as it includes the HeViCs dwarf galaxies (Grossi et al. 2015), the DGS (Cormier et al. 2014), the BCDs not yet published by Hunt et al., and DDO 53, Sextans A, Sextans B and WLM, the extremely metal-poor galaxies studied by Shi et al. (2015), Shi et al. (2016) and Elmegreen et al. (2013). The MAGMA mean $\log(M_{\text{star}}/M_{\odot}) = 9.7$ is ~ 3 times lower than the mean $\log(M_{\text{star}}/M_{\odot}) = 10.2$ of the 158 (including high- z) detections in the Bothwell et al. (2016a) sample; while 30% (124) of the MAGMA galaxies have $M_{\text{star}} \leq 10^{9.3} M_{\odot}$, this is true for

only 7% (11) of the Bothwell et al. (2016a) galaxies, and for $\sim 11\%$ (18) of those in Bothwell et al. (2016b).

Nevertheless, the most important difference between the MAGMA sample and the Bothwell et al. sample(s) is the inclusion of galaxies at high redshift in the latter. As shown in Appendix A, the addition of these galaxies significantly increases the amplitude of the M_{H_2} term in the 4D PCA, and reduces that of SFR. When the $z \sim 2$ galaxies are not included, the results of a 4D PCA on the Bothwell et al. sample are ambiguous, because the metal content is found to increase with increasing SFR, similarly to the increase with M_{star} . However the statistical significance of this result is low, and the sample is ill conditioned because of the behavior of SFR with M_{star} in the sample.

4.3. Methodology comparison and parameter uncertainties

In Appendix B, we assess the consequences of introducing Gaussian noise on an observing sample that is to be subject to a PCA. After constructing several sets of mock samples based on well-defined input scaling relations, we conclude that the accuracy with which the original relations can be retrieved depends on the amount of noise injected. It is fairly common to calculate uncertainties on fitted parameters by injecting noise in a sample and repeating the exercise several times (e.g., Bothwell et al. 2016a,b). However, our results show that this process skews the data because of the broader range in the parameter space, and relative importance of outliers in a PCA.

Another important consideration is the importance of the M_{star} distribution of a sample like the one considered here. At a given level of noise injection σ , we found that the broader the range of M_{star} , the more consistent with the original “true” scaling relations will be the results.

In some sense, as we show in Appendix B, observing samples such as MAGMA already contain noise, and adding more will skew results, compromising reliability. Ultimately, these are the reasons we chose to apply probabilistic PCA and boot-strap PCA with sample replacement, rather than perturb the parameters of the sample by injecting noise.

5. Constraints on metal content and galaxy winds

The tight scatter shown by the MZR is suggestive of an underlying physical process, and many analytical studies and simulations over the last decade have concluded that outflows driven by star formation are the primary agent shaping the MZR (Dalcanton 2007; Erb 2008; Finlator & Davé 2008; Peeples & Shankar 2011; Peeples et al. 2014; Creasey et al. 2015). In particular, there is increasing evidence that metals are removed more efficiently by outflows in low-mass galaxies (e.g., Dalcanton 2007; Finlator & Davé 2008; Spitoni et al. 2010; Chisholm et al. 2018). Outflows are inevitably linked to star formation and gas supply, making MAGMA, with measurements of M_{star} , SFR, O/H, and gas content, an ideal resource for a fresh assessment of the dependence of the MZR on outflows. In the next sections, we derive scaling relations for M_{gas} , and then apply a simple analytical model to assess the mass and velocity dependence of the metal-loading factors for the outflows inferred for the MAGMA sample.

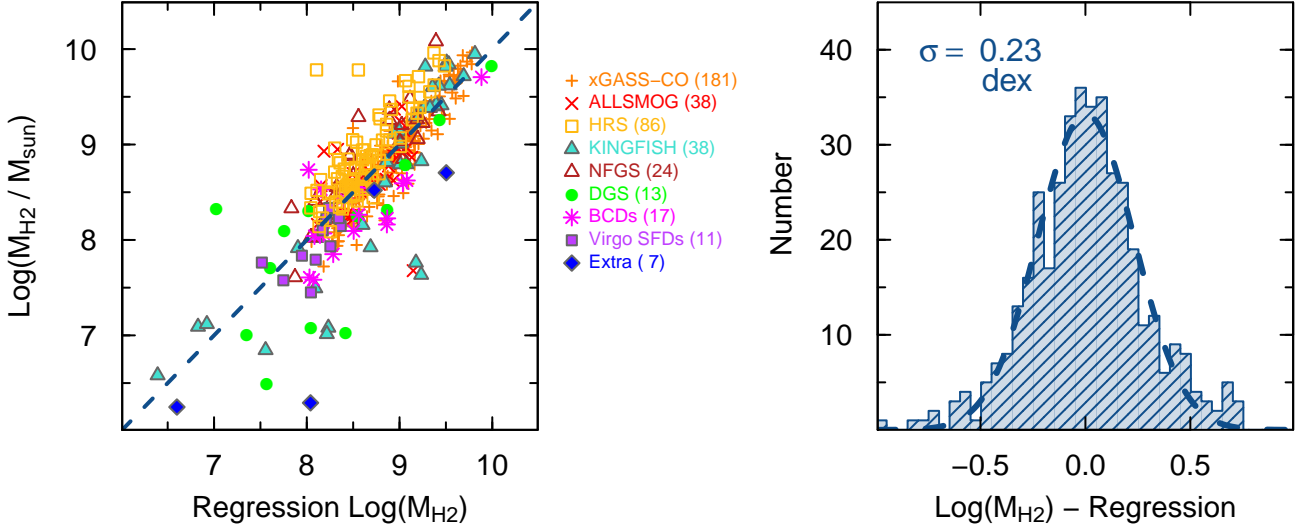


Fig. 8. Observed values of $\text{Log}(M_{\text{H}_2})$ in the MAGMA sample to those predicted by the regression given in Eq. (5). The parent samples of the individual MAGMA galaxies are reported in the legend in the middle panel, and the right panel shows the residuals and the Gaussian fit; the 1σ dispersion of the Gaussian is 0.231 dex as discussed in the text.

5.1. Scaling relations for gas mass

Up to now, we have focused on predicting metallicity, but, with MAGMA, we can also place important constraints on gas content in the Local Universe. In Sect. 3.1, a 4D PCA showed that the four parameters M_{star} , SFR, $12+\log(\text{O}/\text{H})$, and M_{H_2} or M_{gas} are related through a 2D planar relation, with metallicity as the main primary dependent variable. **This implies that O/H depends primarily on M_{star} and SFR, but also that M_{gas} must depend primarily on these two variables because of the physical connection between gas content and metallicity.**

The 3D PCA in Sect. 3.2 confirmed that the three parameters M_{star} , SFR, and $12+\log(\text{O}/\text{H})$, can be expressed through a 2D dependence or planar relation, with O/H as the dependent parameter. The planar nature of the 3D PCA with gas is less clear, although PC3, the principal component with the lowest variance, contains between 5% and 8%, so possibly corresponding to a 2D plane. However, as shown in Table 3, the PC3 gas coefficients (for M_{HI} , M_{H_2} , M_{gas}) are smaller than for SFR, so the inversion of the PC3 relation is problematic. Because the PC3 SFR coefficient is the largest of the three, relative to M_{star} and the gas components, SFR would be considered the most dependent parameter; thus there is not a clear gas dominance as there is for metallicity. This means that the expressions for M_{H_2} or M_{gas} obtained by inverting PC3 would not be reliable, a fact that can also be appreciated by inspecting Table 3 showing particularly large uncertainties for the M_{H_2} coefficients.

Thus, to find an expression for M_{H_2} as a function of M_{star} and SFR, we perform a robust least-squared regression, and find the following relation:

$$\begin{aligned} \log M_{\text{H}_2} = & (0.42 \pm 0.03) \log(M_{\text{star}}) \\ & + (0.50 \pm 0.04) \log(\text{SFR}) + (4.81 \pm 0.30) \end{aligned} \quad (5)$$

This expression is accurate to ~ 0.23 dex, assessed as before for the $12+\log(\text{O}/\text{H})$ residuals, by fitting a Gaussian to the residuals of the fit. For total gas content, $M_{\text{HI}} + M_{\text{H}_2} = M_{\text{gas}}$,

the analogous regression is only slightly noisier (0.30 dex), but with a weaker M_{star} dependence:

$$\begin{aligned} \log M_{\text{gas}} = & (0.24 \pm 0.04) \log(M_{\text{star}}) \\ & + (0.57 \pm 0.04) \log(\text{SFR}) + (7.24 \pm 0.36) \end{aligned} \quad (6)$$

Fig. 8 shows the comparison of predicted (using Eq. 5) and observed values of $(\log)M_{\text{H}_2}$, with the right panel illustrating the deviations from the 3DPCA(M_{H_2}) PCA prediction, together with the fitted Gaussian. The analogous comparison for M_{gas} is not shown; although similar in form, it is somewhat less accurate, but still good to ~ 0.3 dex.

The 3D PCA suggests that gas mass in the Local Universe, and in particular M_{H_2} , depends on only M_{star} and SFR. The accuracy of the prediction is not perfect, ~ 0.3 dex, but there is no evidence in the MAGMA galaxies for a tertiary dependence on metallicity. This is an important result and one that can be compared with predictions from simulations and baryonic cycling models.

Although our results show that M_{gas} and M_{H_2} are more tightly connected to SFR than to M_{star} , modeling the MZR analytically requires relating M_{gas} to M_{star} , in order to better establish the role of gas dilution in shaping the MZR. In the next section, we will use the MAGMA sample to estimate the metallicity-weighted outflow strengths, but first we need to estimate M_{gas} in terms of M_{star} . Figure 9 shows M_{gas} plotted against M_{star} , with the best-fit linear regression¹³ (in units of M_{\odot}) overplotted:

$$\log(1.366 M_{\text{gas}}) = (0.62 \pm 0.03) \log(M_{\text{star}}/10^9) + (9.17 \pm 0.03) \quad (7)$$

This equation gives a fitted σ of 0.38 dex, slightly larger than the regression given in Eq. (6), which is 0.30 dex. Both slope and intercept are roughly consistent with previous work (e.g., Peebles & Shankar 2011; Papastergis et al. 2012;

¹³ This fit for M_{gas} explicitly includes a correction factor of 1.366 for helium (see Caffau et al. 2011).

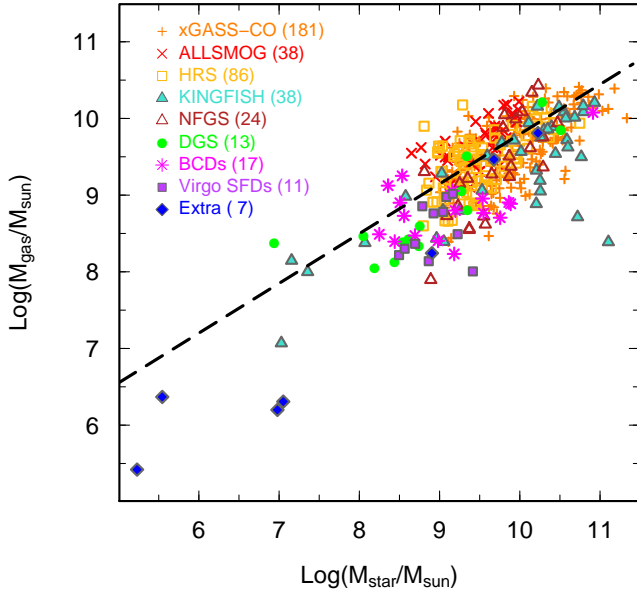


Fig. 9. Observed values of $\text{Log}(M_{\text{gas}})$ vs. $\text{Log}(M_{\text{star}})$ in the MAGMA sample; different symbols correspond to different subsamples as given in the legend in the upper-left corner. The best-fit regression given in Eq. (7) is shown as a long-dashed gray line; the fitted σ of the distribution of residuals is 0.38 dex,

Peeples et al. 2014), although the slope of ~ -0.4 for the gas fraction $F_{\text{gas}} \equiv M_{\text{gas}}/M_{\text{star}}$ is somewhat shallower than ~ -0.5 found by Peeples et al. (2014) on their updated compilation for observed gas content. Although gas fraction is usually defined as gas mass divided by total baryonic galaxy mass $[M_{\text{gas}}/(M_{\text{gas}} + M_{\text{star}})]$, as pointed out by Peeples & Shankar (2011), it is more convenient for the formulation of the metallicity dependence to consider only the fraction with M_{star} . In what follows, the MAGMA gas content M_{gas} will implicitly include the correction factor for helium of 1.366 (Caffau et al. 2011).

5.2. Star-formation driven galaxy outflows and wind loading factors

Galaxies evolve and assemble mass by accreting gas from the intergalactic medium (IGM), forming stars, then expelling gas and metals, thus changing the gas metallicity in the interstellar medium (ISM). Various scenarios have been proposed to describe this baryon exchange cycle relying on, as alluded to above, star-formation driven outflows (e.g., Tremonti et al. 2004; Dalcanton 2007; Erb 2008; Finlator & Davé 2008; Zahid et al. 2014). Here we explore the behavior of the MZR, SFR, and gas content in the MAGMA sample, with the aim of quantifying mass and metallicity loading in stellar outflows, and their impact for shaping the MZR.

The time derivative of a galaxy’s gas metallicity Z_{gas} can be written as:

$$\begin{aligned} \dot{Z}_{\text{gas}} &= \frac{d}{dt} \frac{M_Z}{M_{\text{gas}}} = \frac{1}{M_{\text{gas}}} [\dot{M}_Z - Z_{\text{gas}} \dot{M}_{\text{gas}}] \\ &= \frac{1}{M_{\text{gas}}} \left\{ \text{SFR} [y + Z_{\text{gas}}(\zeta_a - \zeta_w - 1)] - Z_{\text{gas}} \dot{M}_{\text{gas}} \right\} \end{aligned} \quad (8)$$

where y is the nucleosynthetic yield of metals released into the ISM by a stellar population, normalized to the mass of the long-lived stars and remnants. Following Peeples & Shankar (2011), we have defined metal-loading factors ζ_a and ζ_w as:

$$\zeta_a \equiv \left(\frac{Z_{\text{IGM}}}{Z_{\text{gas}}} \right) \frac{\dot{M}_a}{\text{SFR}} = \left(\frac{Z_{\text{IGM}}}{Z_{\text{gas}}} \right) \eta_a \quad (9)$$

and

$$\zeta_w \equiv \left(\frac{Z_w}{Z_{\text{gas}}} \right) \frac{\dot{M}_w}{\text{SFR}} = \left(\frac{Z_w}{Z_{\text{gas}}} \right) \eta_w. \quad (10)$$

where Z_{IGM} , Z_{gas} , Z_w are the metallicities of the IGM, the ISM gas in the galaxy, and the outflow, respectively; \dot{M}_a and \dot{M}_w are the accretion and outflow rates, respectively, so that η_a and η_w are the mass-loading factors, i.e., the accretion and outflow rates normalized by the SFR. ζ_w essentially describes the efficiency with which star-formation-driven outflows remove metals from the galaxy.

Several types of solutions have been proposed for Eq. (8) (e.g., Peeples & Shankar 2011; Dayal et al. 2013; Lilly et al. 2013). Here we adopt the approach of Peeples & Shankar (2011), who have eliminated the time dependence in order to better examine the hypersurface connecting M_{star} , SFR, Z_{gas} , and M_{gas} , and write the solution of Eq. (8) as:

$$\begin{aligned} Z_{\text{gas}} &= y [1 + \zeta_w - \zeta_a + \\ &\quad F_{\text{gas}} (1 - R) \left(\frac{d \log M_{\text{gas}}}{d \log M_{\text{star}}} + \frac{d \log Z_{\text{gas}}}{d \log M_{\text{star}}} \right)]^{-1} \\ &= y [1 + \zeta_w - \zeta_a + \alpha F_{\text{gas}}]^{-1} \end{aligned} \quad (11)$$

where F_{gas} is the ratio of M_{gas} to M_{star} ; α encapsulates the shape of the MZR and the M_{star} dependence of F_{gas}

$$\alpha \equiv (1 - R) \left(\frac{d \log M_{\text{gas}}}{d \log M_{\text{star}}} + \frac{d \log Z_{\text{gas}}}{d \log M_{\text{star}}} \right); \quad (12)$$

R is the mass returned to the ISM when a star dies, with the implicit assumption that stellar lifetimes can be neglected so that R is a net mass return fraction (see e.g., Vincenzo et al. 2016). The implicit assumption here is that the yield y is constant for a given IMF, and that the net mass return R is also constant with time.

Eq. (11) is a powerful tool as it connects the shape of the MZR with relative gas content, and enables us to infer the metal-loading factors of the outflows in the MAGMA sample. To do this, we take the accreting gas Z_{IGM} to be pristine, devoid of metals ($Z_{\text{IGM}} = 0$); this is a typical simplifying assumption (e.g., Dayal et al. 2013; Creasey et al. 2015; Hunt et al. 2016b) and a discussion of the ramifications of this assumption is relegated to a future paper (although see Chisholm et al. 2018). We can then invert Eq. (11) to solve for ζ_w in the MAGMA galaxies. We can do this because we know the shape of the MZR for this sample, and the dependence of F_{gas} on M_{star} , and can thus quantify α . First, oxygen abundance $12 + \log(\text{O}/\text{H})$ is converted to Z_{gas} assuming that oxygen measures the enrichment of a primordial mix of gas comprising approximately 75% hydrogen by mass: $\text{Log}(Z_{\text{gas}}) = \text{Log}(\text{O}/\text{H}) + 0.9560$. Then we fit a cubic

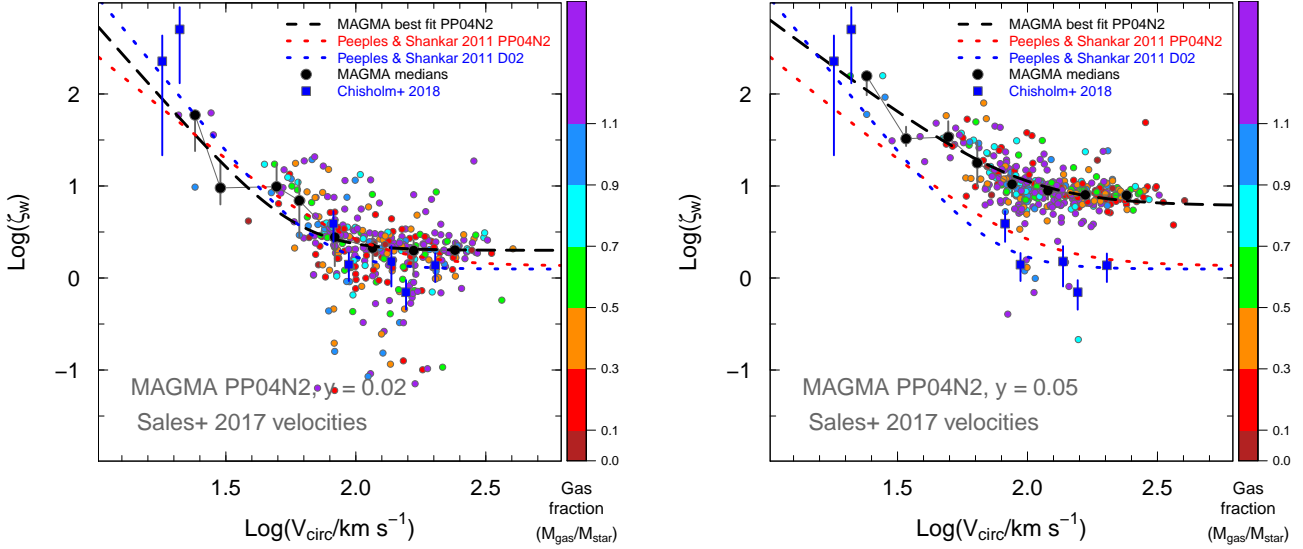


Fig. 10. Log of metal-loading factors ζ_w as a function of virial velocities obtained from the baryonic Tully-Fisher relation as described in the text. The left panel shows MAGMA galaxies with ζ_w calculated using a yield $y = 0.02$, and the right panel using a higher yield $y = 0.05$ as in Vincenzo et al. (2016) for a Chabrier (2003) IMF and the stellar yields by Nomoto et al. (2013). The medians of the MAGMA sample and their quartiles are shown by filled black circles with error bars. Also shown are the galaxies studied by Chisholm et al. (2018), together with the fits of ζ_w as a function of velocity from Peebles & Shankar (2011) and for MAGMA.

polynomial¹⁴ to the MZR shown in Fig. 5:

$$\begin{aligned} \log(Z_{\text{gas}}) = & -2.58 \pm 0.01 + (0.304 \pm 0.017)x + \\ & -(0.0497 \pm 0.007)x^2 - (0.0167 \pm 0.006)x^3 \end{aligned} \quad (13)$$

where $x = \log(M_{\text{star}}/10^9)$. The fit in Eq. (13) gives a residual error of 0.098 dex, identical to the 3DPCA²(OH) fit reported in Eq. (3) and Fig. 7, and discussed in Sect. 3.2. Combining the fits given in Eqs. (13) and (7), and considering that $F_{\text{gas}} = M_{\text{gas}}/M_{\text{star}}$, we evaluate α in Eq. 11, and solve for ζ_w as a function of M_{star} .

Because the outflow strengths probably depend on the depth of the potential well, we can model them in terms of the virial velocities, v_{circ} , as proposed by Peebles & Shankar (2011):

$$\zeta_w = \left(\frac{v_0}{v_{\text{circ}}} \right)^b + \zeta_0 \quad (14)$$

The fits are sensitive to how v_{circ} is calculated, especially for the low-mass galaxies in MAGMA that are beyond the mass regime examined by Peebles & Shankar (2011). We have calculated virial velocities in several ways:

- by inferring halo masses from galaxy M_{star} via halo abundance matching (e.g., Behroozi et al. 2010), with velocities following the formulation presented by Peebles & Shankar (2011);
- with those inferred from empirical baryonic Tully-Fisher relation (BTFR, Lelli et al. 2016);
- with those from the BTFR predicted by APOSTLE/EAGLE simulations from Sales et al. (2017) focused on the low-mass regime.

Because the low-mass end of our sample is somewhat extreme, there is some doubt about the applicability of the usual halo-abundance matching techniques or even the BTFR at such masses. At low M_{star} , and low baryonic masses, the inferred virial velocities change significantly according to whether the relation is linear as in Lelli et al. (e.g., 2016) or inflected at low masses as in Sales et al. (2017). The linear relation gives v_{circ} values that are apparently too low relative to the rest of the sample, while the v_{circ} values by Sales et al. (2017) are more consistent. In any case, our conclusions are independent of what formulation is used to translate from the mass scale to the kinematic one. For samples spanning a large range in M_{star} , the determination of virial velocities is a delicate procedure, especially considering the discrepancies at high M_{star} found by Posti et al. (2018).

Figure 10 shows two calculations of the resulting metallicity-weighted loading factors ζ_w plotted against v_{circ} ; the left panel shows ζ_w using the best approximation to the values of y and R used by Peebles & Shankar (2011), and the right panel ζ_w with the updated yields and mass return fractions given by Vincenzo et al. (2016) for a Chabrier (2003) IMF and the stellar yields from Nomoto et al. (2013). The fits for the MAGMA sample are shown in both panels of Fig. 10, together with the best-fit estimates from the analysis of Peebles & Shankar (2011) for two different metallicity calibrations. For $y = 0.02$, we find $v_0 = 98 \pm 17 \text{ km s}^{-1}$, $b = 2.4 \pm 0.3$, and $\zeta_0 = 0.61 \pm 0.45$; this is not too different from that for the PP04N2 ζ_w fit given by Peebles & Shankar (2011): $v_0 = 112 \text{ km s}^{-1}$, $b = 2.31$, and $\zeta_0 = 1.35$ (see their Table 4). Our fit for the larger yield $y = 0.05$ is significantly different, with $v_0 = 290 \pm 44 \text{ km s}^{-1}$, $b = 1.8 \pm 0.1$, and $\zeta_0 = 4.3 \pm 1.0$. It is clear that the assumed yield y has a strong impact on the shape of the trend of ζ_w with v_{circ} .

With the idea of revealing a trend of ζ_w with gas fraction, $M_{\text{star}}/M_{\text{gas}}$, Fig. 10 encodes this quantity as a color bar. However, there seems to be no clear behavior of ζ_w with

¹⁴ The use of a linear fit gives a slightly larger residual error, but does not change significantly the inference of the outflow properties.

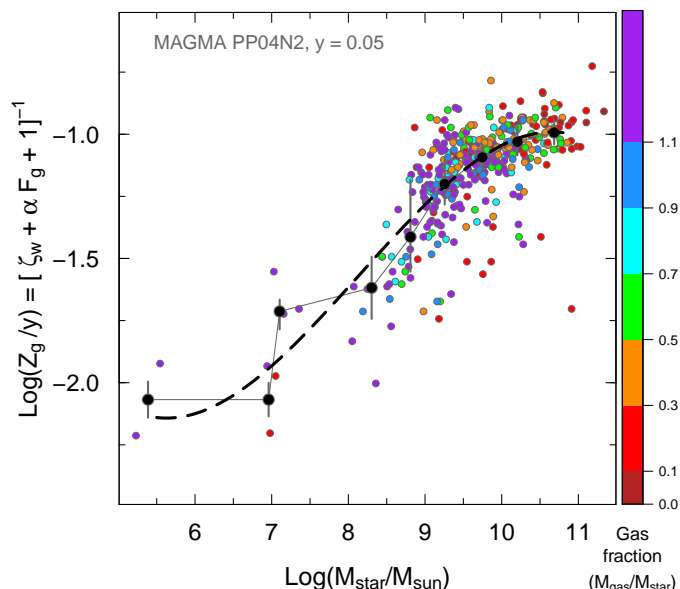


Fig. 11. Log of the metallicities Z_{gas} of the MAGMA galaxies divided by the yield, here using a yield $y = 0.05$. As in Fig. 10, the medians of the MAGMA sample and their quartiles are shown by filled black circles with error bars. Also shown is a cubic fit to the metallicities, as given in Eq. (13), but with the renormalization from $12+\log(\text{O}/\text{H})$ to Z_{gas} described above.

F_{gas} ; neither the high- ζ_w galaxies nor the ones with more moderate ζ_w are unambiguously gas-rich or gas-poor.

Also included in Fig. 10 are measurements of ζ_w from COS observations of ultraviolet absorption lines in 7 galaxies in the Local Universe (Chisholm et al. 2018). By analyzing the underlying stellar continuum, and using the observed line profiles to constrain optical depth and covering fraction, Chisholm et al. (2018) were able to quantify the mass outflow rate, \dot{M}_w (see Eq. 10). Then, by modeling a combination of species to infer the photoionization structure, they obtain column densities of each element, that are used to constrain the metallicity of the outflow Z_w . As shown in Chisholm et al. (2018), their results are well fit by the analytical predictions of Peeples & Shankar (2011), and as we show here, are also consistent with our MAGMA results, as long as y is fairly low. The yields $y \sim 0.05$ predicted by Vincenzo et al. (2016) for the Chabrier (2003) IMF used here are apparently too high to accommodate agreement of MAGMA with the COS results. Indeed, Chisholm et al. (2018) use their results to constrain metal yields, and find values that are lower, more consistent with Salpeter (1955) IMF, even though they based their analysis on Chabrier (2003).

With the formalism of Eq. (11), the yield y affects not only the shape of ζ_w with v_{circ} , but also its amplitude. If gas fractions F_{gas} are too high, then we would infer *negative* values of ζ_w ¹⁵; this is physically unfeasible so that there must be some compromise between measurement errors for F_{gas} and the value we choose for y . With $y = 0.02$, 92 MAGMA galaxies ($\sim 21\%$) have $\zeta_w < 0$; with $y = 0.05$, there are only 9. Given the consistency of MAGMA ζ_w with the results of Chisholm et al. (2018) for a lower yield, we prefer a y value of 0.02 – 0.03, even though we are left with $\sim 20\%$

of the sample with measured F_{gas} that are too high to be consistent with the analytical formulation given in Eq. 11. A refinement of our technique will be the subject of a future paper.

Our analysis of the MAGMA sample confirms on a statistically significant basis that the metal-loading factor ζ_w of star-formation driven outflows scales inversely with virial velocity, or equivalently M_{star} . This implies that metals are more efficiently expelled from low-mass galaxies, than from high-mass ones, independently of the adopted yield or metallicity calibration. Such a conclusion is in good agreement with Torrey et al. (2019) who find that the Illustris-TNG simulations also predict that metal retention efficiency is higher at lower M_{star} . Figure 11 illustrates the analytical approach pursued here, and shows that the MZR is indeed shaped by outflows driven by star-formation processes, as also suggested by much previous work.

6. Summary and conclusions

With the aim of investigating the role of gas on the mass-metallicity relation, we have compiled a new ‘MAGMA’ sample of 415 galaxies covering unprecedented ranges in parameter space, spanning more than 5 orders of magnitude in M_{star} , SFR, and M_{gas} , and almost 2 orders of magnitude in metallicity. All O/H values have been converted to a common metallicity calibration, PP04N2.

Applying both 4D PCAs and piecewise 3D PCAs to MAGMA confirms previous results that O/H can be accurately ($\lesssim 0.1$ dex) described only using M_{star} and SFR. However, our findings contradict earlier versions of PCA dimension reduction on smaller samples, as we find that the O/H depends on SFR more strongly than on either H I or H₂. This is because gas content, in particular M_{H_2} but also total M_{gas} ($M_{\text{H I}} + M_{\text{H}_2}$), can be fairly well estimated (~ 0.3 dex) based only on a linear combination of M_{star} and SFR. Thus, even though a PCA shows mathematically that only a 2D plane is necessary to describe metallicity Z or M_{gas} (or M_{H_2}), the dependence of Z on gas content is not well constrained with a PCA.

Instead, to assess how gas affects the MZR, we have used the MAGMA sample to infer the mass loading and metal-retention efficiency of star-formation driven outflows. For the first time, such an assessment is possible on a single sample with all the necessary measurements: M_{star} , SFR, Z , and M_{gas} . Following the approach outlined by Peeples & Shankar (2011), we have determined the M_{star} dependence of gas fraction F_{gas} ($\equiv M_{\text{gas}}/M_{\text{star}}$), and inferred the metal-loading factors of the outflows ζ_w (see Eq. 11). By fitting our results with an analytical formulation of metal-loading factors as a function of virial velocity, we have found that lower-mass galaxies (with lower v_{circ}) are up to ~ 100 times more efficient at expelling metals than high-mass systems. This confirms previous work, but here with a coherent analysis on a single sample. Fig. 10 shows this result, together with estimates of metal-loading factors from the literature (Chisholm et al. 2018); the agreement is excellent, but is sensitive to the values used for the yields y .

We find that the MZR is shaped by outflows, as shown in Fig. 11, and that metal-retention efficiency changes with stellar mass, as also found by simulations (Torrey et al. 2019). Our assessment confirms earlier efforts, but now with a consistent, statistically significant sample of galaxies in the Local Universe. This is an important result, useful for

¹⁵ The negative ζ_w values have not been included in the fitting procedure to approximate Eq. (14).

constraining models of galaxy evolution. Future work is needed to place these findings in the context of metal pollution in high-redshift galaxy populations, and to quantify changing metal-retention efficiency and its impact on the evolution of metallicity in galaxies.

Acknowledgements

The authors would like to thank A. Baker, F. Belfiore, S. Bisogni, C. Cicone, M. Dessauges-Zavadsky, Y. Izotov, S. Kannappan, R. Maiolino, P. Oesch and D. Schaerer for helpful discussions. We acknowledge funding from the INAF PRIN-SKA 2017 program 1.05.01.88.04. We thank Yong Shi for passing us their results in digital form. We have benefited from the public available programming language Python, including the `numpy`, `matplotlib` and `scipy` packages. This research made extensive use of `ASTROPY`, a community-developed core Python package for Astronomy ([Astropy Collaboration et al. 2013](#)), and `glueviz`, a Python library for multidimensional data exploration ([Beaumont et al. 2015](#)). This research has also made use of data from the HRS project; HRS is a *Herschel* Key Programme utilizing Guaranteed Time from the SPIRE instrument team, ESAC scientists and a mission scientist. The HRS data was accessed through the Herschel Database in Marseille (HeDaM - <http://hedam.lam.fr>) operated by CeSAM and hosted by the Laboratoire d'Astrophysique de Marseille.

References

- Abazajian, K. N., Adelman-McCarthy, J. K., Agüeros, M. A., et al. 2009, *ApJS*, 182, 543
- Accurso, G., Saintonge, A., Catinella, B., et al. 2017, *MNRAS*, 470, 4750
- Andrews, B. H. & Martini, P. 2013, *ApJ*, 765, 140
- Asplund, M., Grevesse, N., Sauval, A. J., & Scott, P. 2009, *ARA&A*, 47, 481
- Astropy Collaboration, Robitaille, T. P., Tollerud, E. J., et al. 2013, *A&A*, 558
- Baldry, I. K., Driver, S. P., Loveday, J., et al. 2012, *MNRAS*, 421, 621
- Baldwin, J. A., Phillips, M. M., & Terlevich, R. 1981, *PASP*, 93, 5
- Beaumont, C., Goodman, A., & Greenfield, P. 2015, in *Astronomical Society of the Pacific Conference Series*, Vol. 495, *Astronomical Data Analysis Software and Systems XXIV (ADASS XXIV)*, ed. A. R. Taylor & E. Rosolowsky, 101
- Behroozi, P. S., Conroy, C., & Wechsler, R. H. 2010, *ApJ*, 717, 379
- Berg, D. A., Skillman, E. D., Marble, A. R., et al. 2012, *ApJ*, 754, 98
- Bigiel, F., Leroy, A., Walter, F., et al. 2008, *AJ*, 136, 2846
- Bisigello, L., Caputi, K. I., Grogan, N., & Koekemoer, A. 2018, *A&A*, 609, A82
- Bolatto, A. D., Wolfire, M., & Leroy, A. K. 2013, *ARA&A*, 51, 207
- Boselli, A., Cortese, L., & Boquien, M. 2014, *A&A*, 564, A65
- Boselli, A., Eales, S., Cortese, L., et al. 2010, *PASP*, 122, 261
- Boselli, A., Fossati, M., Gavazzi, G., et al. 2015, *A&A*, 579, A102
- Bothwell, M. S., Maiolino, R., Cicone, C., Peng, Y., & Wagg, J. 2016a, *A&A*, 595, A48
- Bothwell, M. S., Maiolino, R., Kennicutt, R., et al. 2013, *MNRAS*, 433, 1425
- Bothwell, M. S., Maiolino, R., Peng, Y., et al. 2016b, *MNRAS*, 455, 1156
- Bothwell, M. S., Wagg, J., Cicone, C., et al. 2014, *MNRAS*, 445, 2599
- Brinchmann, J., Charlot, S., White, S. D. M., et al. 2004, *MNRAS*, 351, 1151
- Brown, T., Cortese, L., Catinella, B., & Kilborn, V. 2018, *MNRAS*, 473, 1868
- Caffau, E., Ludwig, H.-G., Steffen, M., Freytag, B., & Bonifacio, P. 2011, *Sol. Phys.*, 268, 255
- Calzetti, D., Wu, S.-Y., Hong, S., et al. 2010, *ApJ*, 714, 1256
- Catinella, B., Saintonge, A., Janowiecki, S., et al. 2018, *MNRAS*, 476, 875
- Chabrier, G. 2003, *Publications of the Astronomical Society of the Pacific*, 115, 763
- Chisholm, J., Tremonti, C., & Leitherer, C. 2018, *MNRAS*, 481, 1690
- Cicone, C., Bothwell, M., Wagg, J., et al. 2017, *A&A*, 604, A53
- Cormier, D., Madden, S. C., Leboutteiller, V., et al. 2014, *A&A*, 564, A121
- Creasey, P., Theuns, T., & Bower, R. G. 2015, *MNRAS*, 446, 2125
- Cresci, G., Mannucci, F., & Curti, M. 2018, *arXiv e-prints* [[arXiv:1811.06015](#)]
- Cresci, G., Mannucci, F., Sommariva, V., et al. 2012, *MNRAS*, 421, 262
- Curti, M., Cresci, G., Mannucci, F., et al. 2017, *MNRAS*, 465, 1384
- Daddi, E., Elbaz, D., Walter, F., et al. 2010, *ApJ*, 714, L118
- Dalcanton, J. J. 2007, *ApJ*, 658, 941
- Dale, D. A., Cohen, S. A., Johnson, L. C., et al. 2009, *ApJ*, 703, 517
- Davé, R., Finlator, K., & Oppenheimer, B. D. 2012, *MNRAS*, 421, 98
- Davies, J. I., Baes, M., Bendo, G. J., et al. 2010, *A&A*, 518, L48
- Dayal, P., Ferrara, A., & Dunlop, J. S. 2013, *MNRAS*, 430, 2891
- De Vis, P., Gomez, H. L., Schofield, S. P., et al. 2017, *MNRAS*, 471, 1743
- Efron, B. 1979, *Ann. Statist.*, 7, 1
- Efron, B. 1982, *The Jackknife, the Bootstrap and other resampling plans*
- Elbaz, D., Dickinson, M., Hwang, H. S., et al. 2011, *A&A*, 533, A119
- Ellison, S. L., Patton, D. R., Simard, L., & McConnachie, A. W. 2008, *ApJ*, 672, L107
- Elmegreen, B. G., Rubio, M., Hunter, D. A., et al. 2013, *Nature*, 495, 487
- Engelbracht, C. W., Rieke, G. H., Gordon, K. D., et al. 2008, *ApJ*, 678, 804
- Erb, D. K. 2008, *ApJ*, 674, 151
- Eskew, M., Zaritsky, D., & Meidt, S. 2012, *AJ*, 143, 139
- Finlator, K. & Davé, R. 2008, *MNRAS*, 385, 2181
- Gil de Paz, A., Silich, S. A., Madore, B. F., et al. 2002, *ApJ*, 573, L101
- Gratier, P., Braine, J., Rodriguez-Fernandez, N. J., et al. 2010, *A&A*, 512, A68
- Graziani, L., de Bressan, M., Schneider, R., Kawata, D., & Salvadori, S. 2017, *MNRAS*, 469, 1101
- Greve, A., Becker, R., Johansson, L. E. B., & McKeith, C. D. 1996, *A&A*, 312, 391
- Grossi, M., Corbelli, E., Bizzocchi, L., et al. 2016, *A&A*, 590, A27
- Grossi, M., Hunt, L. K., Madden, S. C., et al. 2015, *A&A*, 574, A126
- Hastie, T. & Stuetzle, W. 1989, *Journal of the American Statistical Association*, 84, 502
- Huang, M.-L. & Kauffmann, G. 2014, *MNRAS*, 443, 1329
- Hughes, T. M., Cortese, L., Boselli, A., Gavazzi, G., & Davies, J. I. 2013, *A&A*, 550, A115
- Hunt, L., Dayal, P., Magrini, L., & Ferrara, A. 2016a, *MNRAS*, 463, 2002
- Hunt, L., Dayal, P., Magrini, L., & Ferrara, A. 2016b, *MNRAS*, 463, 2020
- Hunt, L., Magrini, L., Galli, D., et al. 2012, *MNRAS*, 427, 906
- Hunt, L. K., De Looze, I., Boquien, M., et al. 2019, *A&A*, 621, A51
- Hunt, L. K., García-Burillo, S., Casasola, V., et al. 2015, *A&A*, 583, A114
- Hunt, L. K., Thuan, T. X., Izotov, Y. I., & Sauvage, M. 2010, *ApJ*, 712, 164
- Hunt, L. K., Weiß, A., Henkel, C., et al. 2017, *A&A*, 606, A99
- Izotov, I. I., Guseva, N. G., Lipovetskii, V. A., Kniazev, A. I., & Stepanian, J. A. 1991, *A&A*, 247, 303
- Izotov, Y. I., Thuan, T. X., & Stasińska, G. 2007, *ApJ*, 662, 15
- Janowiecki, S., Catinella, B., Cortese, L., et al. 2017, *MNRAS*, 466, 4795
- Jansen, R. A., Fabricant, D., Franx, M., & Caldwell, N. 2000, *ApJS*, 126, 331
- Kannappan, S. J., Guie, J. M., & Baker, A. J. 2009, *AJ*, 138, 579
- Kannappan, S. J., Stark, D. V., Eckert, K. D., et al. 2013, *ApJ*, 777, 42
- Kennicutt, Robert C., J. 1998, *ApJ*, 498, 541
- Kennicutt, R. C., Calzetti, D., Aniano, G., et al. 2011, *PASP*, 123, 1347
- Kennicutt, Jr., R. C., Hao, C.-N., Calzetti, D., et al. 2009, *ApJ*, 703, 1672
- Kewley, L. J. & Dopita, M. A. 2002, *ApJS*, 142, 35, (KD02)
- Kewley, L. J. & Ellison, S. L. 2008, *ApJ*, 681, 1183
- Kewley, L. J., Jansen, R. A., & Geller, M. J. 2005, *PASP*, 117, 227
- Kobulnicky, H. A., Dickey, J. M., Sargent, A. I., Hogg, D. E., & Conti, P. S. 1995, *AJ*, 110, 116
- Kobulnicky, H. A. & Kewley, L. J. 2004, *ApJ*, 617, 240

- Kroupa, P. 2001, MNRAS, 322, 231
- Lara-López, M. A., Hopkins, A. M., López-Sánchez, A. R., et al. 2013, MNRAS, 434, 451
- Lelli, F., McGaugh, S. S., & Schombert, J. M. 2016, ApJ, 816, L14
- Lequeux, J., Peimbert, M., Rayo, J. F., Serrano, A., & Torres-Peimbert, S. 1979, A&A, 500, 145
- Leroy, A., Bolatto, A., Walter, F., & Blitz, L. 2006, ApJ, 643, 825
- Leroy, A., Bolatto, A. D., Simon, J. D., & Blitz, L. 2005, ApJ, 625, 763
- Leroy, A. K., Walter, F., Bigiel, F., et al. 2009, AJ, 137, 4670
- Lilly, S. J., Carollo, C. M., Pipino, A., Renzini, A., & Peng, Y. 2013, ApJ, 772, 119
- Madden, S. C., Rémy-Ruyer, A., Galametz, M., et al. 2013, PASP, 125, 600
- Madden, S. C., Rémy-Ruyer, A., Galametz, M., et al. 2014, PASP, 126, 1079
- Maiolino, R., Nagao, T., Grazian, A., et al. 2008, A&A, 488, 463
- Mannucci, F., Cresci, G., Maiolino, R., Marconi, A., & Gnerucci, A. 2010, MNRAS, 408, 2115
- Marble, A. R., Engelbracht, C. W., van Zee, L., et al. 2010, ApJ, 715, 506
- Markarian, B. E. & Stepanian, D. A. 1983, Astrofizika, 19, 639
- Moustakas, J., Kennicutt, Jr., R. C., Tremonti, C. A., et al. 2010, ApJS, 190, 233
- Murphy, E. J., Condon, J. J., Schinnerer, E., et al. 2011, ApJ, 737, 67
- Noeske, K. G., Faber, S. M., Weiner, B. J., et al. 2007, ApJ, 660, L47
- Nomoto, K., Kobayashi, C., & Tominaga, N. 2013, ARA&A, 51, 457
- Oey, M. S., Herrera, C. N., Silich, S., et al. 2017, ApJ, 849, L1
- Papastergis, E., Cattaneo, A., Huang, S., Giovanelli, R., & Haynes, M. P. 2012, ApJ, 759, 138
- Peebles, M. S. & Shankar, F. 2011, MNRAS, 417, 2962
- Peebles, M. S., Werk, J. K., Tumlinson, J., et al. 2014, ApJ, 786, 54
- Pettini, M. & Pagel, B. E. J. 2004, MNRAS, 348, L59
- Posti, L., Fraternali, F., & Marasco, A. 2018, arXiv e-prints [arXiv:1812.05099]
- Rémy-Ruyer, A., Madden, S. C., Galliano, F., et al. 2014, A&A, 563, A31
- Renzini, A. & Peng, Y.-j. 2015, ApJ, 801, L29
- Roweis, S. 1998, in Proceedings of the 1997 Conference on Advances in Neural Information Processing Systems 10, NIPS '97 (Cambridge, MA, USA: MIT Press), 626–632
- Saintonge, A., Catinella, B., Tacconi, L. J., et al. 2017, The Astrophysical Journal Supplement Series, 233, 22
- Saintonge, A., Kauffmann, G., Kramer, C., et al. 2011a, MNRAS, 415, 32
- Saintonge, A., Kauffmann, G., Wang, J., et al. 2011b, MNRAS, 415, 61
- Sales, L. V., Navarro, J. F., Oman, K., et al. 2017, MNRAS, 464, 2419
- Salim, S., Rich, R. M., Charlot, S., et al. 2007, The Astrophysical Journal Supplement Series, 173, 267
- Salpeter, E. E. 1955, ApJ, 121, 161
- Sandstrom, K. M., Leroy, A. K., Walter, F., et al. 2013, ApJ, 777, 5
- Sargent, M. T., Béthermin, M., Daddi, E., & Elbaz, D. 2012, ApJ, 747, L31
- Schmidt, M. 1959, ApJ, 129, 243
- Schruba, A., Leroy, A. K., Walter, F., et al. 2012, AJ, 143, 138
- Shi, Y., Wang, J., Zhang, Z.-Y., et al. 2015, ApJ, 804, L11
- Shi, Y., Wang, J., Zhang, Z.-Y., et al. 2016, Nature Communications, 7, 13789
- Smith, B. J. & Hancock, M. 2009, AJ, 138, 130
- Speagle, J. S., Steinhardt, C. L., Capak, P. L., & Silverman, J. D. 2014, ApJS, 214, 15
- Spitoni, E., Calura, F., Matteucci, F., & Recchi, S. 2010, A&A, 514, A73
- Stark, D. V., Kannappan, S. J., Wei, L. H., et al. 2013, ApJ, 769, 82
- Strange, H. & Zwiggelaar, R. 2015, Intelligent Data Analysis, 19, 1213
- Torrey, P., Vogelsberger, M., Marinacci, F., et al. 2019, MNRAS, 484, 5587
- Tremonti, C. A., Heckman, T. M., Kauffmann, G., et al. 2004, ApJ, 613, 898
- Ugryumov, A. V., Engels, D., Lipovetsky, V. A., et al. 1999, A&AS, 135, 511
- Ugryumov, A. V., Engels, D., Pustilnik, S. A., et al. 2003, A&A, 397, 463
- Vincenzo, F., Matteucci, F., Belfiore, F., & Maiolino, R. 2016, MNRAS, 455, 4183
- Walter, F., Taylor, C. L., Hüttemeister, S., Scoville, N., & McIntyre, V. 2001, AJ, 121, 727
- Wei, L. H., Kannappan, S. J., Vogel, S. N., & Baker, A. J. 2010, ApJ, 708, 841
- Wen, X.-Q., Wu, H., Zhu, Y.-N., et al. 2014, MNRAS, 438, 97
- Wen, X.-Q., Wu, H., Zhu, Y.-N., et al. 2013, MNRAS, 433, 2946
- Wolfire, M. G., Hollenbach, D., & McKee, C. F. 2010, ApJ, 716, 1191
- Wright, E. L., Eisenhardt, P. R. M., Mainzer, A. K., et al. 2010, AJ, 140, 1868
- Xianxi, L., Li, S., Guoquan, L., Menghua, X., & Wei, W. 2017, in 2017 36th Chinese Control Conference (CCC), 9665–9669
- Young, J. S., Xie, S., Tacconi, L., et al. 1995, ApJS, 98, 219
- Zahid, H. J., Dima, G. I., Kudritzki, R.-P., et al. 2014, ApJ, 791, 130
- Zhu, M., Papadopoulos, P. P., Xilouris, E. M., Kuno, N., & Lisenfeld, U. 2009, ApJ, 706, 941
- Zibetti, S., Charlot, S., & Rix, H.-W. 2009, MNRAS, 400, 1181

Appendix A: Details of comparison with previous work: a cautionary tale

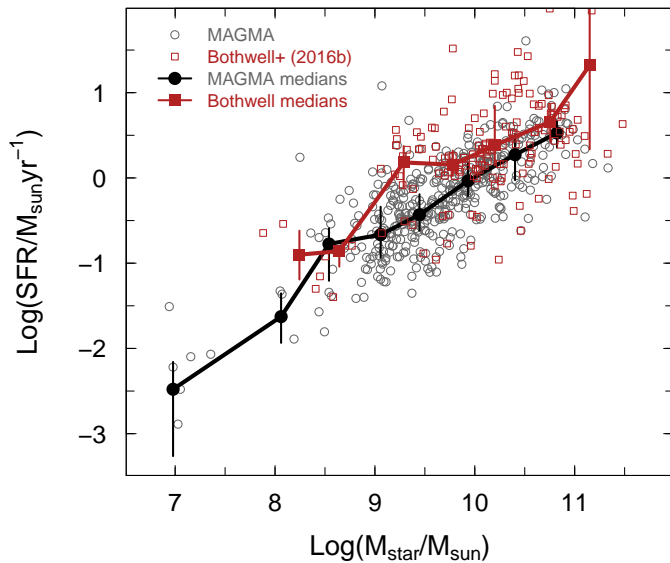


Fig. A.1. $\text{Log}(\text{SFR})$ vs. $\text{Log}(M_{\text{star}})$ for the MAGMA sample as in Fig. 4, but here also plotted are the galaxies from Bothwell et al. (Table 2 in 2016a), together with the 8 galaxies from Hunt et al. (2015) added but with reduced M_{star} as described in the text. Medians for both samples are also shown, but only medians with ≥ 3 points in the respective M_{star} bins are plotted here.

There are two salient differences between the MAGMA sample and the sample from Bothwell et al. (2016b). One is the significant low-mass coverage of the MAGMA sample, and the other is the SFRs. Both these are illustrated in Fig. A.1 where the MS for the two samples are plotted; the median points show only those M_{star} bins with ≥ 3 data points. The Bothwell et al. (2016b) sample is the same as that from Bothwell et al. (2016a), but with 8 BCDs from Hunt et al. (2015); Bothwell et al. (2016b) altered the M_{star} values, and to best approximate their sample, for the BCDs from Hunt et al. (2015) we have arbitrarily lowered the M_{star} values by a factor of three¹⁶. Even with the addition of the BCDs from Hunt et al. (2015), the mass distribution is significantly more extended for MAGMA. The two low-mass bins in the Bothwell et al. sample of Fig. A.1 are the galaxies from Hunt et al. (2015) that are not present in the sample used by Bothwell et al. (2016a), and the highest-mass bin is dominated by the high- z sub-millimeter galaxies (SMGs) and MS galaxies at $z \sim 2$.

There are also differences in the SFRs: while MAGMA adopts COLDGASS galaxies with parameters from Saintonge et al. (2017), Bothwell et al. (2016a,b) use the COLDGASS parameters reported by Saintonge et al. (2011a,b). However, a subsequent study (Huang & Kauffmann 2014) showed that the SFRs in those papers are overestimated by ~ 0.2 dex because of aperture effects from the CO single-dish IRAM beam. Roughly half (115 galaxies) of the Bothwell et al. sample is from COLDGASS which means that these values are also discrepant with respect to MAGMA. This can be seen in Fig. A.1 where, at a given

M_{star} , the Bothwell et al. sample tends to have higher SFRs than MAGMA.

Possibly the most important difference in this context relative to MAGMA is the inclusion by Bothwell et al. of the 17 high- z galaxies (9 main-sequence galaxies and 8 SMGs). These galaxies are at $z \sim 2$, and have significantly higher SFRs than the local galaxies of similar stellar mass, because of the increasing normalization of the star-formation main sequence with redshift (e.g., Speagle et al. 2014). The minimum $\text{Log}(M_{\text{star}}/M_{\odot})$ value in the high- z sample is 9.78, and the mean $\text{SFR} \sim 274 M_{\odot} \text{yr}^{-1}$; for the low- z sample over the same mass range, the mean $\text{SFR} \sim 2.4 M_{\odot} \text{yr}^{-1}$, more than 100 times smaller. A similar difference applies to the ratios of M_{H_2} in the two samples, where the mean M_{H_2} in the high- z sample is ~ 85 times higher than in the low- z galaxies over the same range in M_{star} . To assess the impact of these galaxies on the results by Bothwell et al. (2016a,b), we have performed 4D PCAs on the Bothwell et al. (2016b) sample, with and without the 17 high- z galaxies, using only the galaxies with CO detections in their Table 2 (and Hunt et al. 2015). Results are reported in Table A.1.

The upper part of Table A.1 shows the 4D PCA for H_2 for the Bothwell et al. (2016b) sample including the 17 high- z MS galaxies and SMGs and the 8 BCDs from Hunt et al. (2015). The results are in fairly good agreement¹⁷ with those of Bothwell et al. (2016b). The dependence of $12+\text{log}(\text{O}/\text{H})$ on M_{H_2} is larger than that on SFR; our probabilistic PCA estimates of the uncertainties show, however, that the coefficient for the M_{H_2} dependence is determined with $< 3\sigma$ significance.

The lower part of Table A.1 shows instead the 4D PCA result for the low- z Bothwell et al. (2016a) sample, without the 17 high- z galaxies, but with the 8 BCDs from Hunt et al. (2015). The M_{star} dependence is significantly reduced, the SFR dependence is increased, and the M_{H_2} dependence is consistent with 0.0 to within the errors. Interestingly, the SFR and M_{star} coefficients have the same sign, implying that increasing both SFR and M_{star} will increase Z ; this is contrary to the “normal” 3DPCA¹-OH behavior in which at a given M_{star} , increasing SFR tends to reduce Z . The reason for this seemingly odd behavior is hinted at in Fig. A.1, where the SFR does not increase with M_{star} with the “usual” MS slope. Nevertheless, the comparison in Table A.1 of the two versions of the Bothwell et al. sample, including or omitting the high- z galaxies, shows that the PCA significantly changes, and that the most probable driver of the lack of metallicity SFR dependence relative to M_{H_2} is caused by the inclusion of $z \sim 2$ galaxies which, at a given M_{star} , have a significantly higher molecular gas content and SFR than galaxies in the Local Universe.

Appendix B: Assessment of Monte Carlo error injection on PCA fits

To explore the effect of injecting Gaussian noise on a dataset subject to a PCA, we generated several “mock” samples of

¹⁷ This sample is not quite the same as that analyzed by Bothwell et al. (2016b) because the 8 galaxies from Hunt et al. (2015) are included with an arbitrary factor of 3 lower M_{star} , since Bothwell et al. (2016b) recalculated their M_{star} values but did not tabulate the new M_{star} values. Moreover the numbers of galaxies do not apparently match; here we are analyzing only the 158+8 CO detections given in Table 2 of Bothwell et al. (2016a) with 8 BCDs (with $M_{\text{star}}/3$ from Hunt et al. 2015).

¹⁶ Bothwell et al. (2016b) has used a different technique to estimate M_{star} , and find roughly a factor of 3 times lower values, but there is no tabulation of their modified values.

Table A.1. 4D PCA results for the [Bothwell et al. \(2016b\)](#) sample^a

Method	PC4(1) 12+log(O/H) (KD02)	PC4(2) log ($M_{\text{star}}/M_{\odot}$)	PC4(3) log (SFR/ $M_{\odot} \text{ yr}^{-1}$)	PC4(4) log (M_{H2}/M_{\odot}) ^b	PC4 std. dev.	PC4 proportion of variance	PC3	PCA1+PC2
<i>Including the 17 high-z galaxies and 8 BCDs (166)</i>								
PCA	0.872	-0.408	-0.125	0.242	0.169	0.014	0.042	0.943
PPCA	0.905 ± 0.016	-0.381 ± 0.018	-0.069 ± 0.038	0.165 ± 0.044	0.182	0.017		
PPCA	0.903 ± 0.017	-0.383 ± 0.017	-0.071 ± 0.042	0.167 ± 0.047	0.182	0.017		
BSPCA	0.871 ± 0.028	-0.404 ± 0.027	-0.125 ± 0.042	0.239 ± 0.054	0.167	0.014		
BSPCA	0.865 ± 0.033	-0.405 ± 0.025	-0.131 ± 0.048	0.249 ± 0.062	0.168	0.014		
<i>With 8 BCDs but without the 17 high-z galaxies (149)</i>								
PCA	0.891	-0.378	-0.173	0.186	0.163	0.023	0.074	0.90
PPCA	0.908 ± 0.015	-0.355 ± 0.020	-0.155 ± 0.038	0.145 ± 0.038	0.173	0.027		
PPCA	0.909 ± 0.015	-0.357 ± 0.019	-0.150 ± 0.039	0.142 ± 0.042	0.173	0.027		
BSPCA	0.888 ± 0.033	-0.374 ± 0.039	-0.171 ± 0.046	0.184 ± 0.069	0.159	0.023		
BSPCA	0.886 ± 0.032	-0.378 ± 0.039	-0.169 ± 0.042	0.188 ± 0.066	0.160	0.023		

^a In PCA, the relative signs of the PCs are arbitrary, so that we have used the same conventions for all; this has no bearing on the inversion of the equation of the PC with the least variance.

^b Here M_{H2} is calculated from α_{CO} according to the exponential formulation of [Wolfire et al. \(2010\)](#); [Bolatto et al. \(2013\)](#).

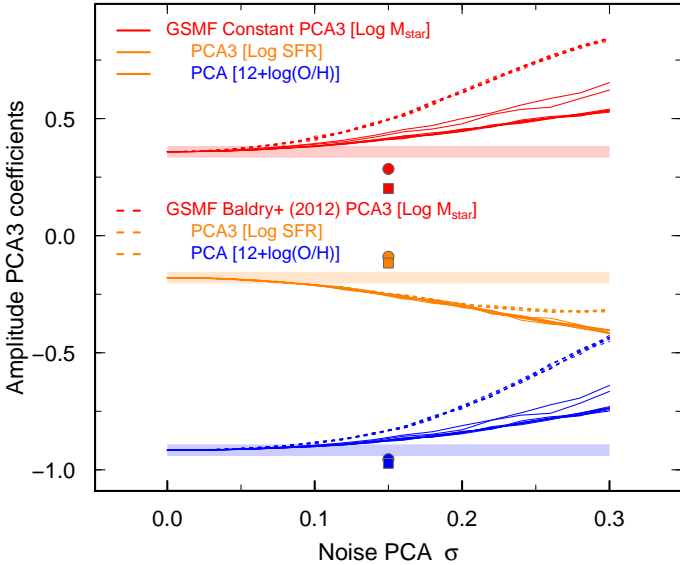


Fig. A.2. 3D PCA coefficients for $\text{Log}(M_{\text{star}})$ (in red), $\text{Log}(\text{SFR})$ (in orange), and $12+\text{log}(\text{O}/\text{H})$ (in blue) plotted against the injected noise level σ ; different line types correspond to the two different M_{star} distributions as described in the text and illustrated in the legend. The different curves for the constant M_{star} case correspond to different lower-mass limits. The true input 3DPCA²(OH) is shown by the transparent lines, with thickness of ± 0.025 dex. The data points (including error bars which are smaller than the symbols) report the PCA coefficients from the initial $\sigma = 0.15$ dex mock sample, but which has been in turn perturbed as described in the text. The aim of this subsequent exercise is to simulate a Monte Carlo perturbation of an observed sample.

the 3DPCA¹-OH for galaxies at $z \sim 0$. To do this, we first

distributed numbers of galaxies in M_{star} bins with redshifts ranging from $z = 0.0$ to $z = 0.02$, according to either a constant M_{star} distribution or one that resembles the GSMF given by [Baldry et al. \(2012\)](#). Within each mass and (small) redshift bin, we selected randomly M_{star} in order to more or less reproduce the assumed distribution. Then we derived a MS of star formation by imposing [Speagle et al. \(2014\)](#) at $z = 0$, or equivalently adopting the relation given by [Hunt et al. \(2019\)](#) for the KINGFISH sample. We added a small (realistic) fraction of starbursts using the formulation of [Sargent et al. \(2012\)](#); this approach separates galaxy populations according to sSFR, and approximates the distribution with two Gaussians. [Sargent et al. \(2012\)](#) further assume that the starburst fraction is independent of mass and redshift, which may or may not be correct (see e.g., [Bisigello et al. 2018](#)). Finally, we related $12+\text{log}(\text{O}/\text{H})$ to M_{star} and SFR via the 3DPCA¹-OH (FPZ) reported by [Hunt et al. \(2016a\)](#). This means that the basic input parameter is M_{star} , which defines SFR through the MS with the addition of a small fraction of starbursts; then $12+\text{log}(\text{O}/\text{H})$ is calculated based on M_{star} and SFR. We adopted a total mock sample size for both M_{star} distributions of $\sim 12\,000$ simulated galaxies.

This construction of the mock samples may seem arbitrary, but in truth the details are not important; we only want to compare what we get out with what we put in, in the case of varying levels of noise injection. To this end, we took this initial “noiseless” sample and introduced varying degrees of Gaussian uncertainty, σ , to SFR and $12+\text{log}(\text{O}/\text{H})$; for simplicity, we used the same value of σ for both SFR and $12+\text{log}(\text{O}/\text{H})$. We repeated this procedure several times, and applied a PCA to each of the noise-injected samples. The results are shown in Fig. A.2, where the 3D PCA coefficients are plotted against the injected noise level σ . The left-hand part of the curves for $\sigma = 0$

are the input values of the 3DPCA¹–OH by which the mock sample was generated. There are seven separate curves in Fig. A.2 for each of the three PCs, corresponding to seven different realizations of the noise injection for the mock samples; the closeness of the curves evident in the figure indicates that the statistical results are quite stable. The discrepant curves for the constant M_{star} case correspond to different lower-mass limits.

The idea here is to simulate an observed sample such as MAGMA, and assess the accuracy of the resulting PCA, compared to the input “true” values. The implicit assumption is that MAGMA, or similar samples, are governed by an underlying 3DPCA¹–OH or 2D plane, but suffer from uncertainty in the measurement of the observables. We cannot know whether or not this is true; we can only ascertain how far the observed data set could differ from the underlying relation if it were present.

Also shown in Fig. A.2 are six data points corresponding to a PCA on the $\sigma = 0.15$ mock sample, but to which an additional perturbation has been applied. We have chosen $\sigma = 0.15$ dex as a starting point, in order to best approximate the behavior of the MAGMA sample which shows a dispersion in $12+\log(\text{O}/\text{H})$ of roughly this amplitude around the best-fit 3DPCA¹–OH. While the original mock samples are intended to reproduce observed samples, this additional injection of Gaussian noise is aimed at simulating a Monte Carlo perturbation of an observed sample. Thus, we injected Gaussian noise of various amplitudes on the variables of our mock sample: $\text{Log}(M_{\text{star}})$ was varied by 0.3 dex; SFR was varied by 30% [corresponding to ~ 0.2 dex on $\text{Log}(\text{SFR})$]; $12+\log(\text{O}/\text{H})$ was varied by 0.1 dex. This is a similar technique to that described by Bothwell et al. (2016a,b), and in principle helps to establish uncertainties in the final PCA results. However, Fig. A.2 shows clearly that the injection of additional noise on the mock sample carries the PCA results even further from the input true 3DPCA¹–OH. The amplitude of the noise injected σ already masks the 3DPCA¹–OH that was the basis for the mock samples, but the additional perturbation exacerbates even more the capacity of the PCA to diagnose the underlying relation.

Fig. B.1 illustrates in another way the process of this subsequent perturbation on the mock sample; the orthogonal projections of the PCs are shown in three different panels. The color maps show the original mock sample with $\sigma = 0.15$ injected Gaussian noise, while the contours show the same data as the individual points (with the GSMF from Baldry et al. 2012), but here with the PCs calculated according to the loadings of the original mock sample. This is done to highlight the change in orientation relative to the original sample, thus illustrating that the injection of additional noise alters the orientation of the components. This can be seen in particular in the upper right panel which compares PC3, dominated by O/H, to PC2, which is dominated by M_{star} , and to a lesser extent SFR; the contours are oriented at a different angle relative to the underlying color map.

We conclude that:

- The injection of Gaussian noise in a noiseless sample changes the PCA characteristics, because of the resulting change of the orientation of the derived PCs (see the curves in Fig. A.2). Further injection of Gaussian noise moves the PCA even further from the input re-

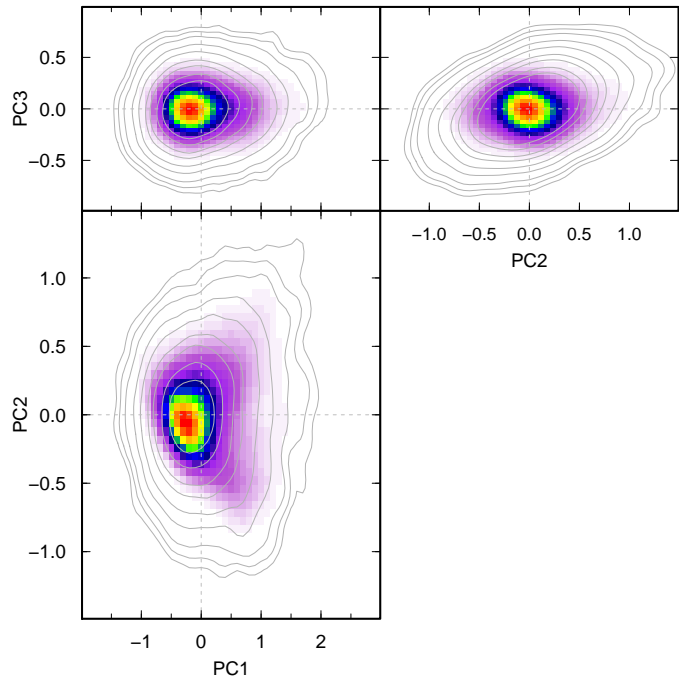


Fig. B.1. 3D PC components under various projections. The underlying color maps show the density distribution of data points with the PCA calculated from the original mock sample with $\sigma = 0.15$ dex, and the contours the density distribution of the perturbed sample but with the PCA loadings of the original one. The change of orientation of the PC decomposition introduced by the perturbation is evident, especially in the upper right panel.

lation, as shown by the individual points in Fig. A.2. Even though the introduction of noise does not change the means of the parameters, it skews the orientation because PCAs consider the entire distribution of data, including outliers.

- The distribution of M_{star} in a sample also impacts the results of a PCA (see varying curves in Fig. A.2). This is because a PCA calculates the orthogonal distance from an orientation, and requires a broad distribution in parameters in order to better take into account eventual outliers.

Ultimately, because of the mathematical nature of the PCA, the addition of noise to a sample for which a PCA is to be performed is deleterious for the reliability of the results. For this reason, we have preferred here to use resampling techniques, rather than alter the noise characteristics of the sample.